AIAA-2013–2066

19th AIAA/CEAS Aeroacoustics Conference

May 27–29, 2013/Berlin, Germany

Hybrid RANS/LES Simulations for Aerodynamic and Aeroacoustic Analysis of a Multi-Element Airfoil

Bastian Nebenführ*, Huadong Yao*, Shia-Hui Peng*† and Lars Davidson*

Abstract

A hybrid RANS/LES modeling approach is used for simulating the turbulent flow around a three-element airfoil in high-lift configuration. A detailed analysis of the flow is made, based on the simulation outcome. A comprehensive aeroacoustic analysis involving all three elements of the airfoil is also presented. To provide input data for acoustic analogies, the results of the simulation are sampled at a permeable stationary surface near the airfoil and at the airfoil itself. The far-field noise signature of the high-lift airfoil is computed with the help of the Kirchhoff integral surface method, the Ffowcs-Williams and Hawkings method for a stationary, permeable surface, and the Curle method. The sound pressure level spectrum exhibits a broad-banded shape with several narrow-banded tonal peaks at low Strouhal numbers. The broad-banded peak at high Strouhal numbers, which is typically associated with vortex shedding behind the blunt slat trailing edge, was also captured. Using Curle's acoustic analogy, the noise emission pattern of the three elements is explored, isolated from each other, revealing that both slat and flap act as dipoles. By refining the used grid, the flow results are significantly improved in terms of slat shear layer instability and resolved turbulent content as compared to our previous work.

I. Introduction

During the take-off and approach and landing phases of a typical flight, so-called high-lift devices are deployed on the airplane's wings to compensate for the lower lift force at the reduced airspeed compared to cruising conditions. The high-lift devices also allow efficient operation (that is, without stall) at higher angles of attack (AoA) than with a clean airfoil. A typical high-lift airfoil consists of a leading edge slat, a main airfoil and one or several trailing edge flaps. While the flaps create most of the additional lift, the slat is deployed to avoid flow separation on the suction side of the main wing element. If this flow separation occurs, it can lead to stall, which stands for a sudden loss of lift force and is hence a safety risk.

A consequence of deploying high-lift devices at airfoils is not only the increase in lift force but also an increased generation of flow-induced noise, which is referred to as airframe noise. This is an undesirable, yet unavoidable, side effect of today's high-lift devices. In fact, with the introduction of new High-Bypass-Ratio engines, engine noise may be considerably reduced. Consequently, the noise created by the high-lift system can match or even exceed the engine noise, particularly during approach and landing. As airports tend to neighbor urban areas, noise emissions from starting and landing aircraft have become a societal problem. To protect residents from aircraft noise, more and more stringent noise emission regulations have been imposed on the aircraft industry.[1] Noise reduction of entire aircraft, and in particular high-lift devices, is hence a challenge of great industrial interest.

Research on the prediction and reduction of airframe noise stemming from the high-lift system has been carried out in many ways. Traditionally, wind tunnel experiments on isolated wings[2,3,4] or aircraft scale models[3,4,5] have been conducted. Some fly-over noise measurements of an Airbus A340 were also performed.[6] More recently, numerical predictions were made using computational fluid dynamics (CFD).[7,8,9,10] Often

*Chalmers Technical University, Department of Applied Mechanics, Gothenburg, Sweden

†Swedish Defence Research Agency (FOI), Stockholm, SE-16490, Sweden

only the near-field noise signature is investigated numerically, as in,[11] but some authors also computed the far-field noise.[7,8]

It is now widely acknowledged that the slat in particular dominates the noise signature of typical high-lift wings.[2,3,12,11,13] Because of that, much effort has focused on the investigation of slat noise and slat noise sources.[14,3,15,16,11,8] Two main noise generation mechanisms were identified at the slat, the noise generation caused by instabilities of the shear layer at the slat cusp and the vortex shedding behind the blunt trailing edge of the slat. Many research groups have investigated the influence of the slat inclination angle[7,17,14] and the state of the boundary layer on the slat.[18] Khorrami et al.[14] found in their numerical study that the vortex shedding behind the slat occurred only for a slat inclination of 30°. When testing a slat inclination of 20°, however, the vortex shedding disappeared. They attributed a strong tonal noise at frequencies of about 40 kHz to the vortex shedding. Singer and co-workers[7] later used the unsteady data from Khorrami's computations for far-field noise prediction based on the Ffowcs-Williams and Hawkings method. They could give further evidence that the far-field noise spectrum of the case with 30° slat deflection indeed featured a strong tonal noise at frequencies between 38 and 45 kHz depending on the slat trailing edge thickness, whereas this tonal peak was not observed for the 20° case. It should be noted that the tonal peak at such high frequencies is of little practical interest, since it is not audible for the human ear.

Computational aeroacoustics (CAA) is dependent on the availability of time-dependent and accurate information about the fluctuating flow field. Direct numerical simulation (DNS) and large-eddy simulation (LES) would be ideal for providing the required input but are out of the reach in wall-bounded flows of industrial interest. At the same time, traditional Reynolds-averaged Navier-Stokes (RANS) simulations fail to provide the necessary unsteady information for aeroacoustic analysis. Common practice today is to use hybrid RANS/LES methods, which are able to combine the advantages of both LES and RANS, and are able to accurately represent fluctuating flow properties on the one hand and to efficiently model the boundary layers on the other. A multitude of approaches has emerged in the past, of which the most prominent is so-called Detached-Eddy Simulation (DES), proposed by Spalart.[19] The idea in DES is to use RANS in the attached boundary layer, where it is well-adjusted and evaluated, and to use LES in separated flow regions. In the separated regions, the flow is dominated by large-scale turbulence, which can be efficiently resolved using LES, even on a coarse mesh.

Phenomena that are always present in flows around wings in high-lift configuration are, among others, laminar-turbulent boundary layer transition, free shear layers, wakes, thick boundary layers and the interaction of these. Furthermore, flow separation over the flap can already occur at moderate AoA. The presence of the above mentioned phenomena makes the flow around a high-lift configuration very complex. It is important to take into account and accurately represent all the flow characteristics, because failure in predicting one of the phenomena may compromise the prediction of another phenomenon. The integrity of the entire simulation is consequently jeopardized. Hence, this complexity makes the flow around a high-lift airfoil a challenging test case for the evaluation of turbulence modeling. Deck[20,21] recently demonstrated the feasibility of a hybrid RANS/LES modeling approach for the prediction of high-lift flows. In his simulations, he employs a zonal DES approach in which designated DES and RANS zones are specified by the user.[22] Choudhari and Khorrami[11] and Lockard and Choudhari[8] have also used a hybrid RANS/LES approach. Essentially, they use unsteady RANS with Menter's SST $k-\omega$ model[23,24] in their computations. To eliminate the highly dissipative effects of the turbulence model, the turbulence production term was switched off in the slat cove region. The strategy can thus be interpreted as similar to a zonal implicit LES.[25,26,27]

The present work investigates the turbulent flow around a multi-element airfoil with deployed high-lift devices. A decoupled strategy is chosen for the aeroacoustic assessment. A turbulence resolving simulation using an algebraic hybrid RANS/LES model[28,29] is made to accurately compute the flow field and provide the instantaneous and non-linear input data required for the acoustic calculations. Based on the input data from the flow simulation, the far-field noise signature is predicted with the help of three different acoustic analogies: the Kirchhoff integral method,[30] the Ffowcs-Williams and Hawkings method[31,32] for a stationary, permeable surface and Curle's method.[33] A comparative study of the results obtained with the different acoustic analogies is given. Unlike most research in the literature, the present work specifically accounts for the noise generated by all three elements and not only by the slat. Using the acoustic analogy of Curle makes it possible to explore the noise emission behavior of the isolated elements. Besides predicting the far-field noise signature of the present high-lift airfoil, the performance of the algebraic hybrid RANS/LES model for predicting turbulent high-lift flow is also assessed.

II. Test case description

The DLR F15 three-element high-lift airfoil is studied as a typical example of an airfoil in high-lift configuration. The same geometry has previously been investigated in the LEISA (Low noise Exposing Integrated design for Start and Approach) project[12,13] at DLR (German Aerospace Center). During the course of this project, an experimental campaign was carried out in the atmospheric low-speed wind tunnel (DNW-NWB) in Braunschweig, Germany, which resulted in experimental surface pressure data. More recently, the same geometry has been a test case in the ATAAC (Advanced Turbulence Simulation for Aerodynamic Application Challenges) EU project and was calculated by numerous partners.

II.A. Hybrid RANS/LES computation

The investigated airfoil consists of a main wing with a leading edge slat and a trailing edge flap. The deflection angles of the slat and the flap are 28.8° and 38.3°, respectively, which gives rise to the anticipation of narrow-banded tonal noise, as found by, for example, Khorrami et al.[14] All trailing edges of the three elements of the airfoil are blunt, except for the slat cusp, which is artificially sharpened.

Numerical simulations of the DLR F15 airfoil have been made using a hybrid RANS/LES approach. The method uses an algebraic mixing-length model in the RANS region, which is combined with the Smagorinsky model[34] in the LES region. Due to its simple algebraic nature and the absence of a transport equation for modeled turbulent quantities, the model can be referred to as a zero-equation hybrid model. In the following, the model will be termed HYB0.[28,29]

In contrast to the wind tunnel measurements, the airfoil is here simulated at free flight, i.e. without the influence of the wind tunnel side walls. The wind tunnel tests were carried out at an AoA of $\alpha = 7.05°$, which had to be corrected numerically in order to take into account the blockage stemming from the flow separation on the wind tunnel side walls. This correction was done in terms of altering the AoA in RANS simulations so as to match the experimental surface pressure distribution. A detailed study using different RANS models and investigating, among other things, the effect of the AoA and transition specification is presented by Nebenführ et al.[35] According to the RANS simulations, a corrected AoA of $\alpha = 6°$ has been chosen for the hybrid RANS/LES simulations. Furthermore, the transition from laminar to turbulent boundary layers is controlled on all three elements. More specifically, the upper and lower surfaces of the slat are treated as laminar, which is in agreement with the findings of Storms et al.,[18] who observed that, above a slat inclination of 19°, the slat boundary layer remained laminar. However, transition locations are specified on the pressure and suction sides of the main wing as well as on the suction side of the flap. The freestream Mach number and chord-based Reynolds number are $M_\infty = 0.15$ and $Re_\infty = 2.1 \times 10^6$, respectively.

In a previous work,[36] computations were made with the HYB0 model on the same geometry, and the importance of the grid resolution in the $x-y$ plane was pointed out in particular. Hence, a refined grid was generated and is used in the present work. The grid is of a hybrid character using hexahedral cells near the walls in order to resolve the boundary layers and using tetrahedral cells away from the wall. The geometry under consideration is a two-dimensional wing section of a generic aircraft used in the LEISA project; the grid was hence first built in a 2D plane. The two-dinal slice consists of about 200000 grid points in the $x-y$ plane. In order to create three-dimensionality, 160 of those 2D grid slices are lined up equidistantly in the spanwise direction over a distance of 16% of the stowed chord length, C. The resulting three-dimensional wing section is unswept, and the grid consists of a total of 32×10^6 grid points with a spanwise resolution of $\Delta z/C = 0.001$. In the far-field, the boundary of the domain is located at a distance of 100 C from the airfoil. Periodic boundary conditions are employed in the spanwise direction.

A timestep of $\Delta t = 5 \times 10^{-6}$ s was employed in the simulation in order to ensure a CFL number based on the maximum speed of an acoustic wave, $(U_\infty + a)$, of $CFL < 4$ in the slat cove region.

Table 1. Information about computational cases

Case	Grid	N [10^6]	$\Delta x_{min}/C$	L_z	$\Delta z/C$	Model
Case1	original (3D)	32	0.0015	0.16 C	0.001	HYB0 model
Case2	refined (3D)	32	0.0005	0.16 C	0.001	HYB0 model
Case3	original (2D)	0.2	0.0015	—	—	SST RANS

All results presented in Section III were obtained with the HYB0 model on the refined grid (Case2), as

mentioned above. For comparison, some results from an older computation with the same hybrid RANS/LES model on the original, but coarser grid (Case1), will also be included. Along with the two turbulence resolving computations, the velocity profiles of a 2D RANS with Menter's SST $k-\omega$ model[23,24] are also presented as a reference (Case3). Details on the different cases are given in Table 1.

A permeable integral surface is included in the grid to enable analysis of the far-field sound via the acoustical analogies of Kirchhoff and Ffowcs-Williams and Hawkings. The surface follows the geometry quite closely and then stretches about 6 C downstream of the flap trailing edge in order to include the noise created by the separated flow behind the airfoil. The distance of the surface from the airfoil is chosen in a way that it includes all the acoustical sources stemming from the core flow region. This is ensured by investigating the vorticity magnitude of a precursor RANS calculation according to the method proposed by Yao et al.[9] In the downstream direction, the integral surface is kept open in order to reduce the artificial noise induced by vortices passing through the surface.

II.B. Acoustic Analogies

In acoustics, the interest is usually in the noise that is radiated to a far-field observer. As the present case can be understood as the situation of a landing airplane, the observers would most likely be residents close to an airport. The typical distance from the plane to the ground will vary during approach and landing but will be in the order of a couple of hundreds of meters.

At present, it is popular to decouple the acoustic analysis from the flow computation. Initially, CFD is used to provide the near-field flow solution, which includes all the noise sources and captures the non-linear flow effects. In a second step, acoustic analogies are used to compute the noise radiation to the far-field observers. As acoustic analogies, the Kirchhoff surface integral method,[30] the Ffowcs-Williams and Hawkings method[31,32] for a stationary permeable surface, and the Curle method for a stationary solid surface[33] have been employed. A brief description of these acoustic analogies follows.

II.B.1. Kirchhoff surface integral method

Kirchhoff's theory[37] was originally used to describe electromagnetic waves. Later, Kirchhoff's formula has been exploited for acoustical problems on stationary and moving integral surfaces.[30] In Kirchhoff's method, all non-linear effects of the acoustical sources are assumed to be enclosed by a permeable integral surface. While all acoustic sources are enclosed by the surface, the flow field outside the surface satisfies the linear condition so that the homogeneous wave equation is fulfilled. With the help of generalized derivatives,[30,32] the Kirchhoff equation for a stationary surface[38] reads as follows:

$$\bar{\Box}^2 p'(\vec{x},t) = -\frac{\partial p'}{\partial n}\delta(f) - \frac{\partial}{\partial x_i}[p' n_i \delta(f)] \tag{1}$$

In Eq. (1), generalized derivatives are denoted by an overbar, such as for the wave operator in $\bar{\Box}^2$, $\delta(f)$ is the Dirac delta function, f is the surface itself and n_i denotes the components of the unit normal vector pointing outwards from the surface. A solution to Eq. (1) can be found via the Green function in free space.

$$\begin{aligned} p'_K(\vec{x},t) = &\frac{1}{4\pi}\int_{f=0}\left(\frac{\cos\theta}{R^2}[p'(\vec{y},t)]_\tau - \frac{1}{R}\left[\frac{\partial p'(\vec{y},t)}{\partial n}\right]_\tau\right. \\ &\left. + \frac{\cos\theta}{c_0 R}\left[\frac{\partial p'(\vec{y},t)}{\partial \tau}\right]_\tau\right) dS \end{aligned} \tag{2}$$

where R denotes the distance to the observer, i.e. $R = |\vec{r}| = |\vec{x}-\vec{y}|$, $\cos\theta = (r_i/R)n_i$, c_0 is the speed of sound and $[\,]_\tau$ indicates that the term is evaluated at retarded time, $\tau = t - R/c_0$. In the present analysis, the three terms of the surface integral will be treated as three individual surface integrals.[10]

$$p'_{1,K}(\vec{x},t) = \frac{1}{4\pi}\int_{f=0}\left(\frac{\cos\theta}{R^2}[p'(\vec{y},t)]_\tau\right) dS \tag{3a}$$

$$p'_{2,K}(\vec{x},t) = -\frac{1}{4\pi}\int_{f=0}\left(\frac{1}{R}\left[\frac{\partial p'(\vec{y},t)}{\partial n}\right]_\tau\right) dS \tag{3b}$$

$$p'_{3,K}(\vec{x},t) = \frac{1}{4\pi}\int_{f=0}\left(\frac{\cos\theta}{c_0 R}\left[\frac{\partial p'(\vec{y},t)}{\partial \tau}\right]_\tau\right) dS \tag{3c}$$

The three terms represent the noise that results from pressure fluctuations, the gradient and the time derivative of the pressure fluctuations, respectively.

II.B.2. Ffowcs-Williams and Hawkings method (FWH) for a stationary, permeable surface

The acoustic analogy developed by Ffowcs-Williams and Hawkings[31] was derived for solid surfaces moving at an arbitrary speed, v_n. Here, the special case of a stationary and permeable surface is used, which can easily be extracted from Brentner's formulation[32] by setting $v_n = 0$.

Brentner and Farassat[32] rewrote the compressible Navier-Stokes equations with the help of generalized functions into a generalized wave equation with non-linear source terms, which is also called the FWH-Equation (Eq. (4)).

$$\begin{aligned}\bar{\Box}^2 p'(\vec{x},t) = &-\frac{\partial}{\partial x_i}[(p'\delta_{ij} + \rho u_i u_j) n_j \delta(f)] \\ &+ \frac{\partial}{\partial t}[\rho u_j n_j \delta(f)] \\ &+ \frac{\bar{\partial}^2}{\partial x_i x_j}[T_{ij} H(f)]\end{aligned} \tag{4}$$

where $T_{ij} = (p' - \rho' c_0^2)\delta_{ij} - \tau_{ij} + \rho u_i u_j$ is the Lighthill tensor,[39,40] δ_{ij} is the Kronecker delta and $H(f)$ is the Heaviside function. As described for the Kirchhoff method, we assume the surface to enclose the entire core flow region. Because of that assumption, it is possible to neglect the volume integral including the Lighthill tensor for the FWH method. A solution to Eq. (4) can be found, once again, based on Green's function for free space.

$$\begin{aligned}p'_F(\vec{x},t) = &-\frac{1}{4\pi}\frac{\partial}{\partial x_i}\int_{f=0}\left(\frac{1}{R}[p'\delta_{ij} + \rho u_i u_j]_\tau n_j\right) dS \\ &+ \frac{1}{4\pi}\frac{\partial}{\partial t}\int_{f=0}\left(\frac{1}{R}[\rho u_i n_j]_\tau\right) dS\end{aligned} \tag{5}$$

The above solution to the FWH equation is the one originally derived for solid surfaces neglecting the volume integral. In this formulation, the first and second integrals can directly be understood in physical terms as the loading and the thickness noise, respectively.[41,32] When a permeable surface is used, the terms lose their physical meaning and it is hence legitimate to write them as individual integrals, as in Yao et al.[10] In Eq. (6), it is then possible to interpret the three terms as the perturbations of pressure, momentum and mass through the surface, respectively,

$$p'_{1,F}(\vec{x},t) = \frac{1}{4\pi}\int_{f=0}\left(\frac{1}{R}\cos\theta\left[\left\{\frac{1}{c_0}\frac{\partial}{\partial\tau} + \frac{1}{R}\right\}p'\right]_\tau\right) dS \tag{6a}$$

$$p'_{2,F}(\vec{x},t) = \frac{1}{4\pi}\int_{f=0}\left(\frac{1}{R}\lambda_{ij}\left[\left\{\frac{1}{c_0}\frac{\partial}{\partial\tau} + \frac{1}{R}\right\}(\rho u_i u_j)\right]_\tau\right) dS \tag{6b}$$

$$p'_{3,F}(\vec{x},t) = \frac{1}{4\pi}\int_{f=0}\left(\frac{1}{R}n_j\left[\frac{\partial}{\partial\tau}(\rho u_j)\right]_\tau\right) dS \tag{6c}$$

where $\lambda_{ij} = (r_i/R)n_j$.

II.B.3. Curle's method for a stationary solid surface

Curle's method can be regarded as a generalization of Lighthill's analogy[39,40] in the presence of stationary solid walls. Introducing generalized variables into the compressible Navier-Stokes equations and rewriting them in terms of a wave equation with non-linear source terms, leads to the following:

$$\begin{aligned}\bar{\Box}^2 p'(\vec{x},t) = &-\frac{\partial}{\partial x_i}[p' n_i \delta(f)] \\ &+ \frac{\bar{\partial}^2}{\partial x_i x_j}[T_{ij} H(f)]\end{aligned} \tag{7}$$

The solution to the Curle equation is given by the free space Green function as

$$p'_C(\vec{x},t) = -\frac{1}{4\pi}\frac{\partial}{\partial x_i}\int_{f=0}\left(\frac{1}{R}[p']_\tau n_i\right)dS + \frac{1}{4\pi}\frac{\bar{\partial}^2}{\partial x_i x_j}\int_V\left(\frac{1}{R}[T_{ij}]_\tau\right)dV \tag{8}$$

The surface integral in Eq. (8) stands for the pressure fluctuations on the solid wall caused by the turbulent boundary layer. The second term represents the impact of the fluctuating stresses on the sound field. However, this term has been neglected owing to its numerically difficult evaluation. Thus only the first term of Eq. (8) is included in the present analysis. We then obtain the total noise for the Curle analogy in the form presented by Yao and co-workers.[9,10]

$$p'_C(\vec{x},t) = \frac{1}{4\pi}\int_{f=0}\left(\frac{1}{R}\cos\theta\left[\left\{\frac{1}{c_0}\frac{\partial}{\partial\tau}+\frac{1}{R}\right\}p'\right]_\tau\right)dS \tag{9}$$

It is noteworthy that Eq. (9) is the same as Eq. (6a) in the present formulation of the FWH approach. Hence, the FWH approach falls back to Curle's method, if a solid, stationary surface is regarded.

III. Results and discussion

This section first presents aerodynamic results. These are followed by an aeroacoustic analysis.

III.A. Aerodynamic analysis

III.A.1. Instantaneous flow

Computations were initially performed with the HYB0 model on the original grid, which showed that the shear layer emanating from the slat cusp showed strongly delayed instabilities.[36] The first Kelvin-Helmholtz instabilities could be observed only at about half the way to the impingement point on the lower wall of the slat trailing edge. This phenomenon was partly blamed on insufficient grid resolution in the $x-y$ plane and partly on the so-called "gray area" problem in hybrid RANS/LES methods. At the interface between RANS and LES, a gray area can be found in which the computation can neither be considered RANS nor LES. The gray area issue isdescribed for instance by Spalart.[42] In order to highlight the grid influence, a new grid with a refined slat cove region was used here. Figure 1 depicts isosurfaces of the Q-criterion for the slat shear layer. The development of Kelvin-Helmholtz instabilities sets in almost immediately after the slat cusp, represented by the roll-up of coherent vortical structures in the spanwise direction. However, the coherent structures are transformed into full three-dimensional turbulence rather late. This delay in secondary instabilities can be attributed to the gray area and must be addressed in terms of hybrid RANS/LES modeling rather than in terms of grid refinement. Generally, the grid refinement led to much richer resolved turbulence structures inside the recirculation zone of the slat cove. It can be seen that the structures are incorporated to some extent in the recirculating flow in the slat cove, whereas the remainder of the structures is ejected from that zone through the gap between the slat and the main wing. Due to a significant flow acceleration in this region, the structures are stretched into long streamwise tubes. Vortex shedding from the blunt slat trailing edge can also be identified in Fig. 1. Figure 2 shows the z-component of the instantaneous vorticity at a mid-span cutplane. A considerable delay in the formation of instabilities can be observed, which again should be addressed in terms of modeling.

III.A.2. Mean flow

The flow, as presented in Fig. 3, exhibits the topology of a typical flow around a high-lift airfoil. There are two recirculating regions in the slat cove and in the cove of the main wing. Besides that, flow separation occurs at this AoA on the flap, as can be observed in Fig. 3(b).

Experimental data are available for validation in the form of the pressure distribution around the airfoil's elements. The following plots contain a comparison between these experimental data and the simulation results. Please note that, due to confidentiality, the absolute pressure levels on the y-axis had to be omitted. Included in Figs. 4 and 5 are the results from both Case1 and Case2. Figure 4 includes all three elements, and

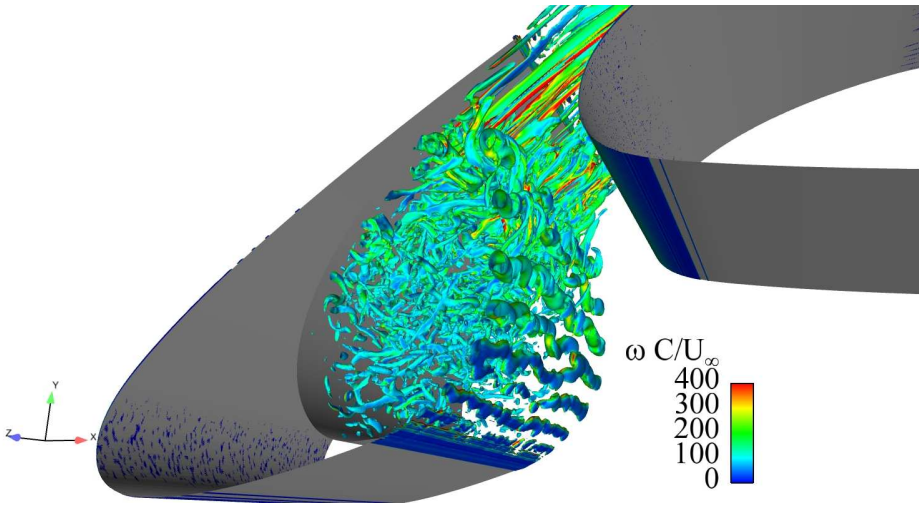

Figure 1. Isosurfaces of the Q-criterion for the free shear layer behind the slat cusp. $\frac{QC^2}{U_\infty^2} = 5000$. Coloring by vorticity magnitude.

it can be seen that generally good agreement with the experiments is achieved for all elements in both cases. The only exception is the suction peak on the main wing, for which the pressure is somewhat underpredicted on both grids. This indicates that the prediction for the flow acceleration through the slat/wing gap too strong. Figure 5 provides a closer look at the pressure distributions around the slat and the flap. It reveals that the predictions of the pressure distributions around the slat are almost identical. Case2 gives an only marginally better estimation of the pressure around the slat. The separated region on the suction side of the flap is represented better in Case2, i.e. Case1 suggests a plateau towards the trailing edge of the flap.

The streamwise component of the mean skin friction coefficient, $C_{f,x}$, is depicted in Fig. 6. Case1 and Case2 report similar distributions around all the elements, except for the suction side of the main wing, where Case2 predicts consistently higher values. This is attributable to a higher turbulent content in the boundary layer for Case2, which might stem from the interaction of the slat wake with the boundary layer. Figure 6(b) indicates that separation on the flap occurs at $x/C = 1.025$ for Case1, whereas it occurs slightly downstream at $x/C = 1.035$ for Case2.

Time-averaged flow quantities are extracted and compared at several locations around the slat and flap, as presented in Figure 7. As mentioned above, previous simulations show strongly delayed instabilities of the free shear layer detaching from the slat cusp.[36] Hence, particular attention was paid to the treatment and development of that shear layer. Figure 8 displays a comparison of modeled and resolved shear stresses, $\overline{u_n' u_s'}$, for Case1 and Case2. It can be seen that the amounts of resolved stresses exceeds the modeled ones at all stations along the slat shear layer (locations given in Fig. 7(a)), except at the first one. Moreover, comparing the HYB0 simulations on the two grids, it can be seen that Case2 enables the resolution of greater shear stress levels. Because higher stress levels are resolved, greater levels of turbulent kinetic energy in the slat shear layer are also resolved with the Case2 grid. Evidence of this is seen in Fig. 9(a), which shows the development of resolved turbulent kinetic energy along the shear layer from the slat cusp to the impingement point at the lower surface of the slat trailing edge. The curve exhibits that k_{uv} increases linearly with increasing distance from the slat cusp. A further, non-linear increase, is shown only near the impingement point ($s/s_{max} = 1$). This can be attributed to the complex flow situation around the impingement location, as highlighted in Fig. 1. Note that the kinetic energy displayed is based on the normal stresses in the x- and y-directions only, i.e. $k_{uv} = \sqrt{\overline{u'u'} + \overline{v'v'}}$. This enables better comparison with computational and experimental results in the literature. Lockard and Choudhari[8] present a numerical investigation of a similar multi-element airfoil. They show in a plot similar to Fig. 9(a) that the turbulent kinetic energy based on the normal stresses in all three directions, i.e. k_{uvw}, does not increase linearly from the slat cusp. In the present case, however, the normal stress in the spanwise direction is so weak in the initial shear layer that there is virtually no difference between the curves of k_{uv} and k_{uvw}. Deck[21] reports that he obtained levels of resolved turbulent kinetic energy in the first half of the slat shear layer of about 2% for the same geometry using the Zonal DES (ZDES)[22] approach. Lockard and Choudhari[8] also show levels of $k_{uv}/U_\infty^2 \approx 0.02$ in the shear layer for

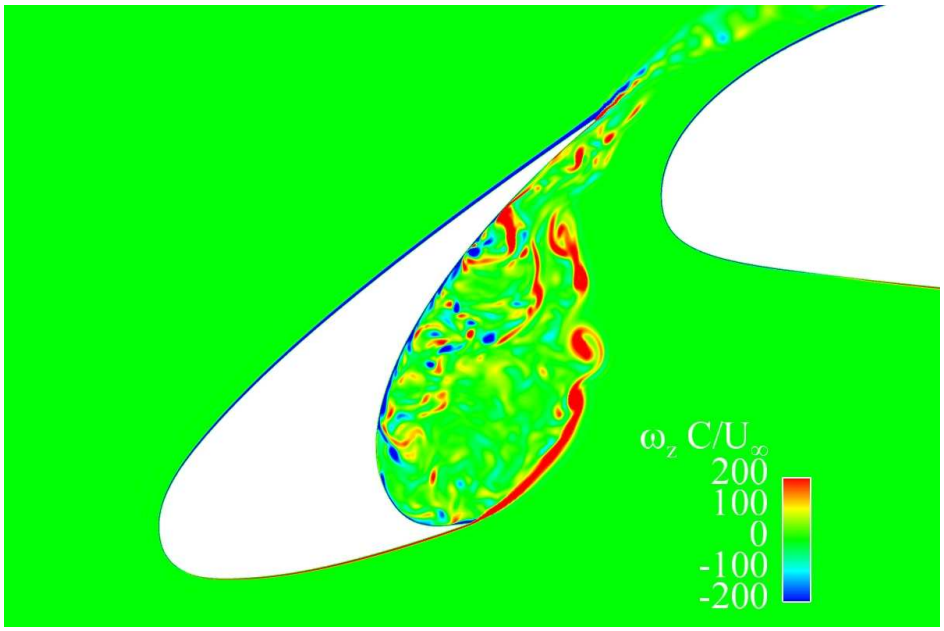

Figure 2. z-component of the normalized, instantaneous vorticity, $\frac{\omega_z C}{U_\infty}$, in the slat cove

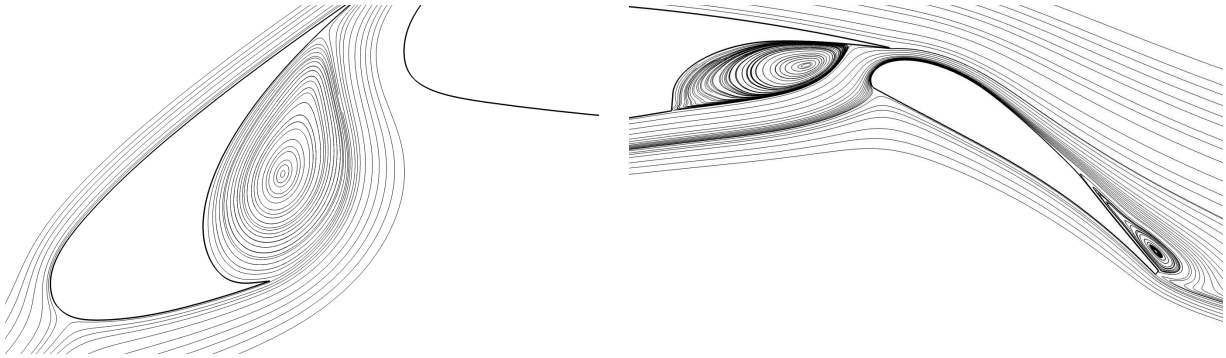

(a) slat (b) flap

Figure 3. Flow pattern around the three-element airfoil, visualized by streamlines

simulations of a similar geometry. The observations of Deck and of Lockard and Choudhari are in agreement with the PIV measurements of Jenkins et al.[15] on a similar high-lift configuration. Figure 9(b), displays contours of the turbulent kinetic energy in the slat cove. Apart from the magnitude in the shear layer, they are in generally good agreement with the results published by Deck,[21] Lockard and Choudhari[8] and Jenkins et al.[15]

The ratio of turbulent viscosity to molecular viscosity, μ_t/μ, is depicted in Fig. 10 to further highlight the superiority of Case2 over Case1 in terms of scale resolving capabilities. A lower turbulent viscosity enables the hybrid RANS/LES model to resolve scales more quickly (i.e. the resolved scales are less damped) and hence leads to a faster onset of shear layer instabilities. Case2 consistently exhibits lower levels of turbulent viscosity, except for the peak at the beginning of the shear layer.

Mean streamwise velocity profiles are extracted at locations F1 – F4 around the flap, and a comparison of Case1, Case2 and Case3 is shown in Fig. 11. At location F1, shortly upstream of the main wing trailing edge, the flow is strongly influenced by the slat wake and its interaction with the attached boundary layer of the main wing. Case2 yields a velocity profile similar to that of the RANS simulation, except for an obvious dent at $y/C \approx 0.007$. This dent is caused by the interface between the hexahedral near-wall grid and the unstructured tetrahedral grid in the off-wall region. However, as there is no evidence of the effect of this erroneous velocity profile at the next downstream location, it is assumed that the overall accuracy

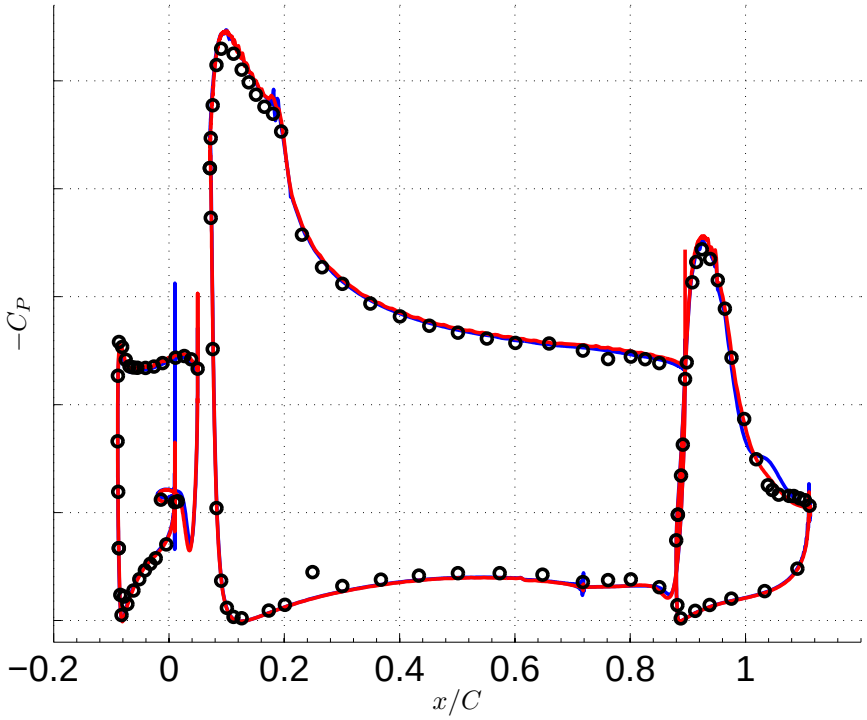

Figure 4. Mean pressure distribution for all elements. ——: Case1, ——: Case2. ○: Experiments. $\Delta C_P = 1$

of the simulation is not compromised. Moreover, it can be seen that the velocity profiles of the turbulence resolving simulations are not as full as the RANS profile. At location F2, the profiles are almost identical for the hybrid RANS/LES simulations. As a result of the flow acceleration through the gap between the main wing and the flap, very thin boundary layers are present at the leading edge of the flap. This was predicted very well by all simulations. Consistent with the findings at location F1, Case3 predicts the highest velocity near the wall. The kink in the profiles at $y/C \approx 0.01$ is the velocity deficit caused by the wake of the main wing. It is most pronounced in the profiles of Case1 and Case2. The velocity deficit can also be identified at the next downstream location. All three computations yield different profiles with different velocity deficits and boundary layer thicknesses. At the most downstream location, the flow has separated from the surface and created a zone with reversed flow, which is indicated by the negative streamwise velocity. The RANS simulation shows the thickest recirculation zone, which can be interpreted as a larger separation bubble compared to the hybrid RANS/LES simulations. Case1 still predicts a larger recirculation zone than Case2, which could already be expected from the skin friction distribution in Fig. 6(b).

It was noted that the velocity profiles in Fig. 11(a) appear to be not as full as the one produced by the SST RANS model. A possible cause can be the so-called Modeled Stress Depletion (MSD), which appears due to grid refinement at the trailing edge of the main wing. The grid becomes fine enough to trigger the switch from RANS to LES mode of the HYB0 model, and the eddy viscosity is subsequently reduced from RANS levels to SGS levels. This is shown in Fig. 12(b) at a streamwise location of $x/C \approx 0.85$. Along with the reduction of eddy viscosity, the modeled stresses are also degrading, which is highlighted in Fig. 12(a). It can also be seen that the resolved stresses are not able to instantly replace the modeled ones. In severe cases, this problem can lead to so-called grid induced separation (GIS), which has been investigated by Menter.[43,24] However, in the present case, this behavior is not necessarily undesirable, as the HYB0 model will have switched to LES mode already when the trailing edge is reached. In principle, this should limit the delay in the formation of shear layer instabilities. Furthermore, the skin friction plot in Fig. 6(a) reveals that no premature separation occurs at the suction side of the main wing at $x/C \approx 0.85$.

Data on spanwise two-point correlations at three locations in the slat cove region are presented in Fig. 13. The locations P1 – P3 are given in Fig. 7(a) and are located directly downstream of the slat cusp, near the free shear layer and in the gap between slat and wing, respectively. A previous study[36] investigated the impact of the spanwise domain extent and found that, even with a spanwise extent of $0.16C$, the spatial

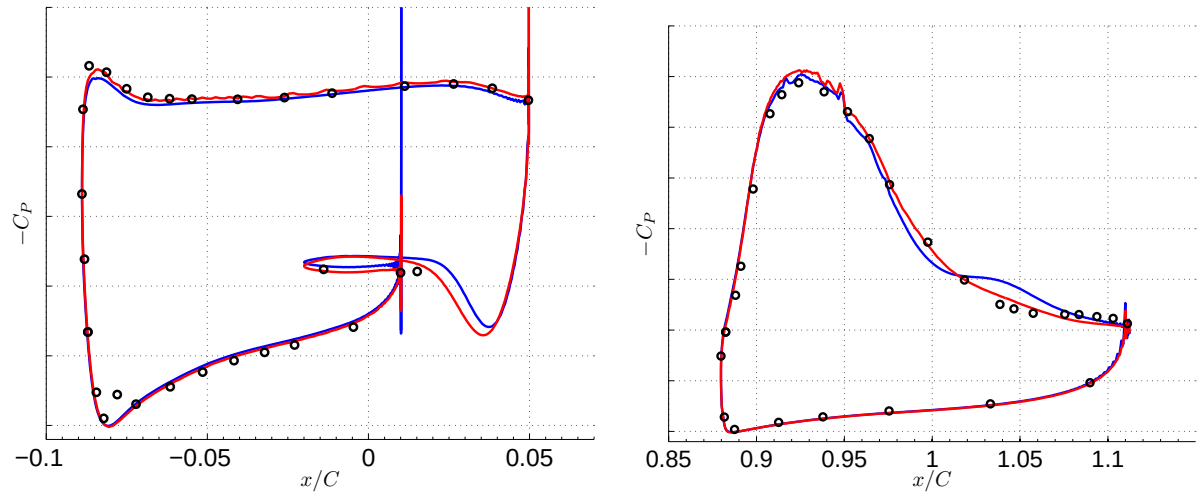

(a) slat (b) flap

Figure 5. Mean pressure distribution around slat and flap. ——: Case1, ——: Case2. ○: Experiments. $\Delta C_P = 1$

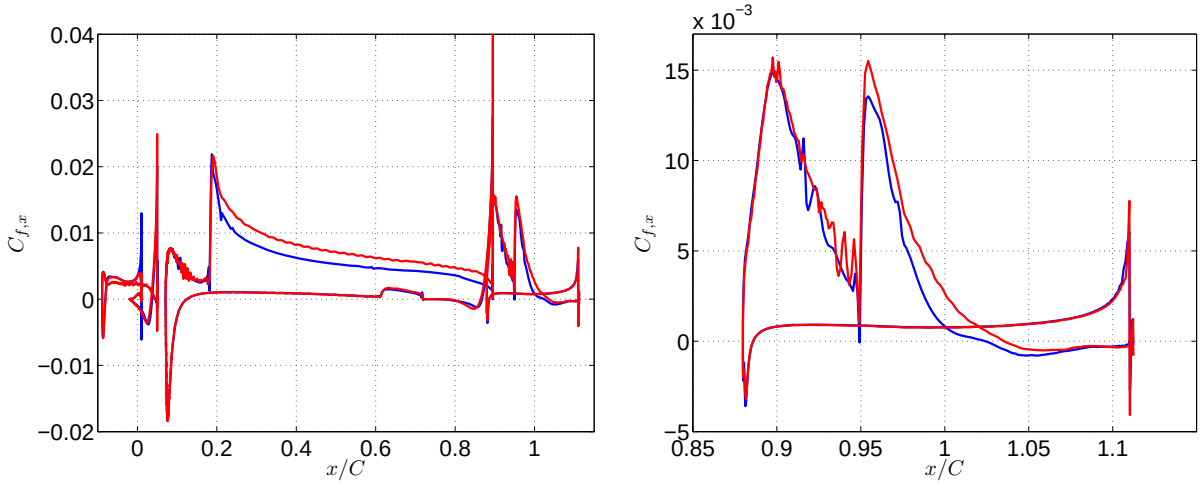

(a) all elements (b) flap

Figure 6. x-component of the mean skin friction coefficient, $C_{f,x}$, for all elements (a) and the flap only (b). ——: Case1, ——: Case2.

correlations were strong. This was blamed partly on the grid resolution in the $x-y$ plane and partly on the sampling locations for the two-point correlations themselves, which are placed in regions of strong flow acceleration in which the flow might undergo relaminarization. Here, however, the sampling locations are kept the same. Note alse that the spanwise grid resolution is the same in Case1 and Case2. Figure 13 reveals that the two-point correlations drop considerably faster and to lower values within the domain for Case2. One can clearly see the effect of the grid resolution in the $x-y$ plane on the flow in the spanwise direction. Using the finer grid of Case2, it is possible to resolve smaller structures, which help to destroy the large structures that were found in Case1 (not presented here). Nevertheless, a larger spanwise domain extent would be desirable. In particular, the two-point correlation of the pressure fluctuations is of some concern.

The markers on the lines represent the spanwise grid resolution. It can be observed that, if the two-point correlations drop to 0, they do so within at least 7 cells. This is a useful piece of information, as it shows that at least 7 spanwise cells are used to resolve the largest scales. Davidson[44] recommends a minimum of 8 cells to resolve the largest scales in a coarse LES. Hence, the spanwise grid resolution can be deemed borderline for the present study.

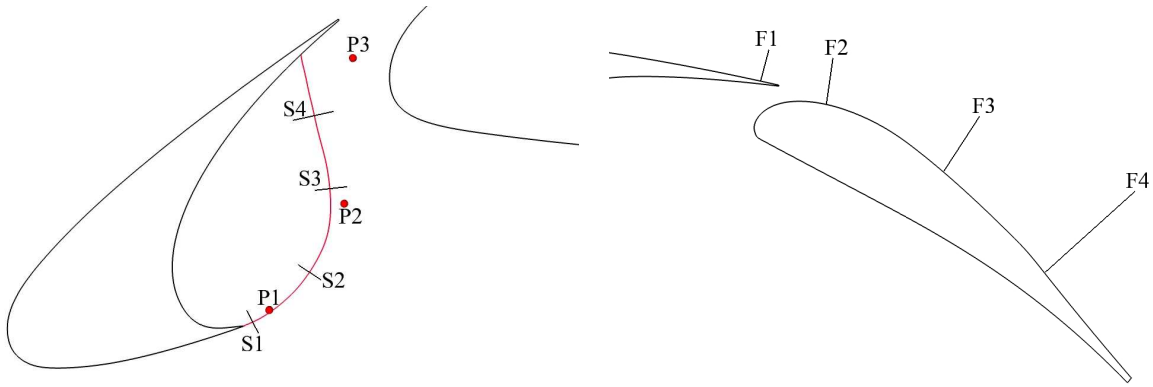

(a) slat (b) flap

Figure 7. Locations for mean data extraction. At the slat (a), S1 − S4 are cross-sections of the shear layer, P1 − P3 are lines in spanwise direction for plotting the two-point correlations and the red line along the shear layer is a spline, at which data was extracted. At the flap (b), F1 − F4 are the locations of the velocity profiles.

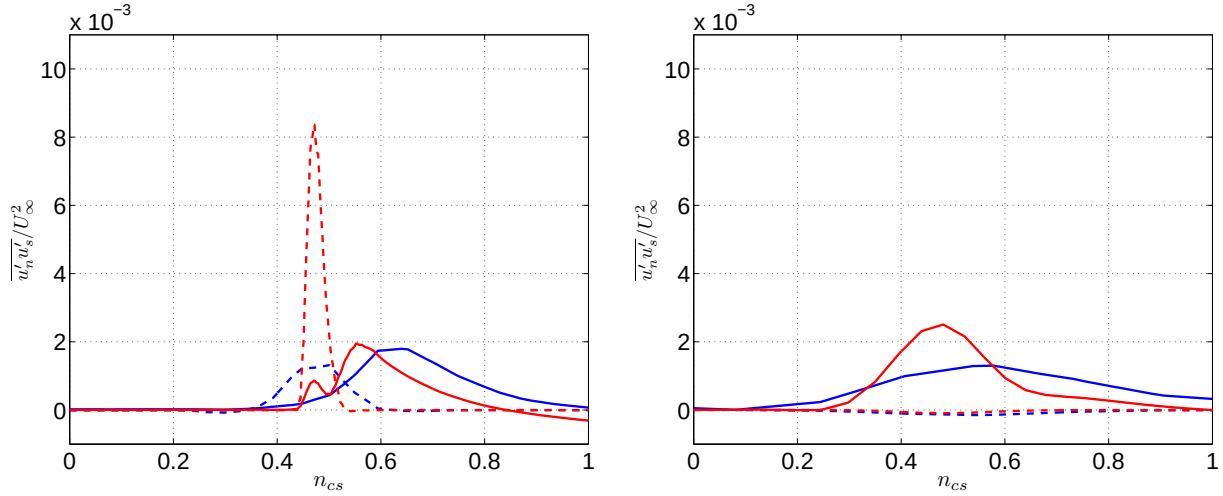

(a) Location S1 (b) Location S2

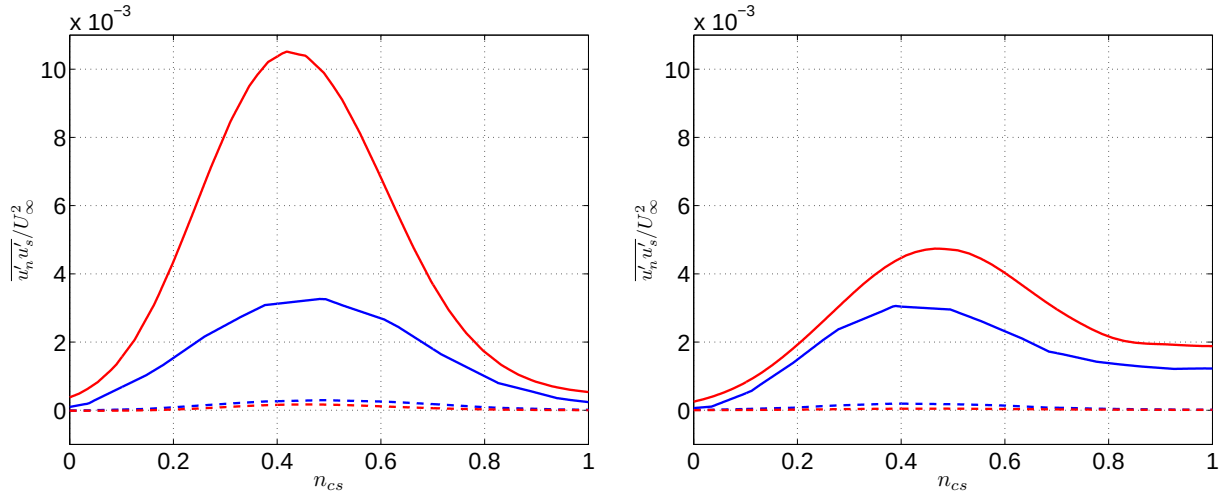

(c) Location S3 (d) Location S4

Figure 8. Resolved (solid lines) and modeled (dashed lines) shear stress, $\overline{u_n' u_s'}$, where n and s denote the normal and tangential direction to the shear layer. ——: Case1, ——: Case2. n_{cs} denotes the coordinate along the shear layer cross-section.

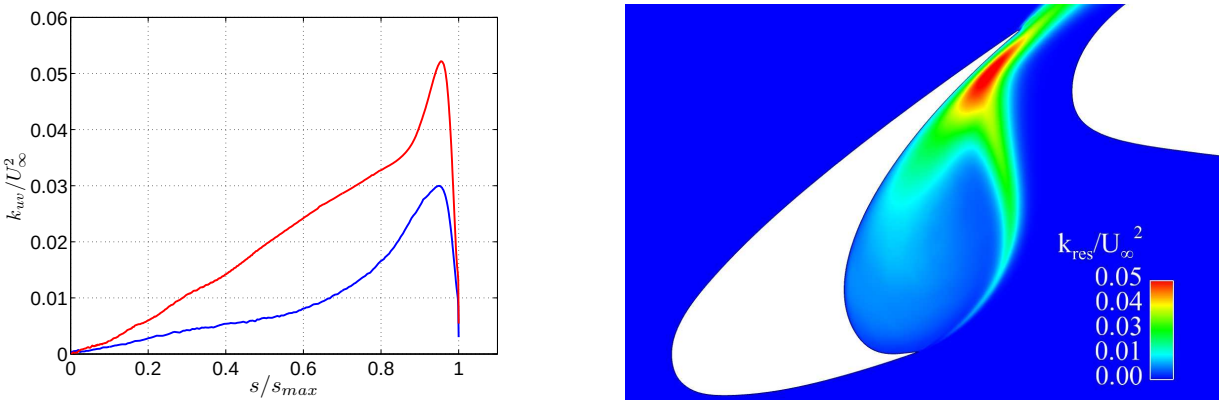

(a) (b)

Figure 9. Resolved turbulent kinetic energy in the slat cove. (a) Development of k_{uv} along the shear layer. ——: Case1, ——: Case2. s/s_{max} denotes the position along the shear layer from the slat cusp. (b) Contours of k_{uv} for Case2.

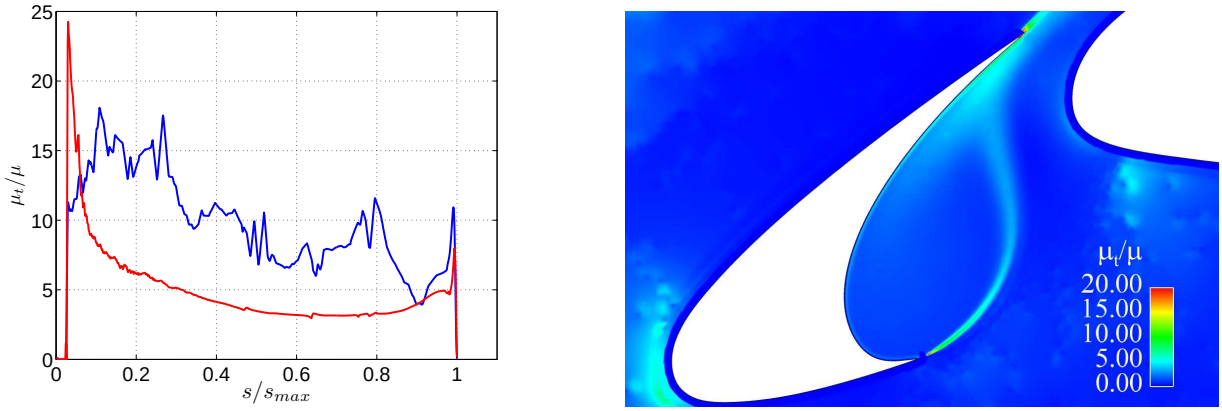

(a) (b)

Figure 10. Viscosity ratio in the slat cove. (a) Development of μ_t/μ along the shear layer. ——: Case1, ——: Case2. s/s_{max} denotes the position along the shear layer from the slat cusp. (b) Contours of μ_t/μ for Case2.

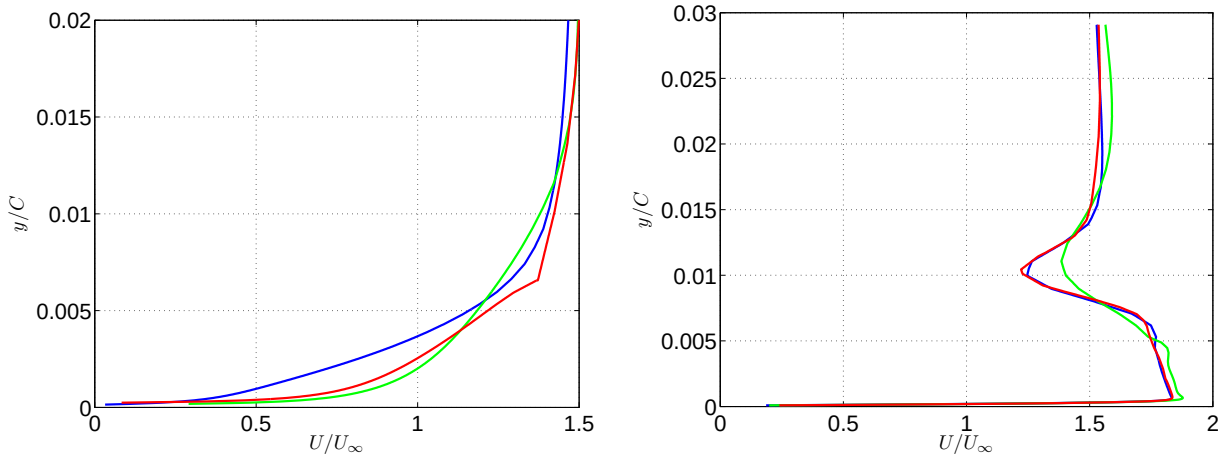

(a) Location F1

(b) Location F2

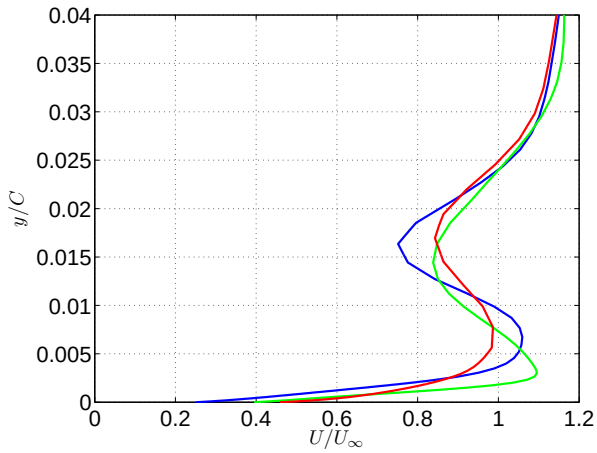

(c) Location F3

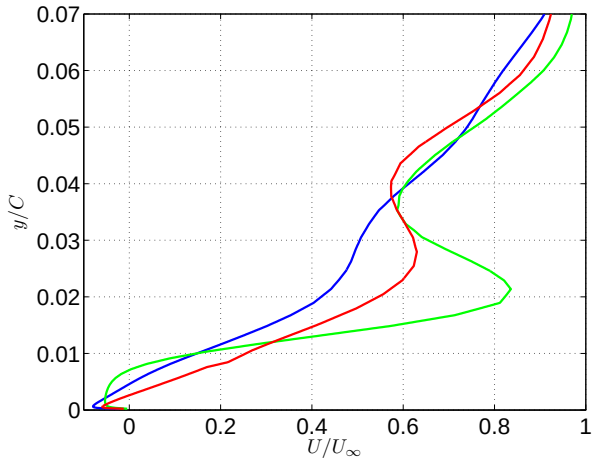

(d) Location F4

Figure 11. Profiles of normalized streamwise velocity, $\frac{|U|}{U_\infty}$. ——: Case1, ——: Case2, ——: Case3.

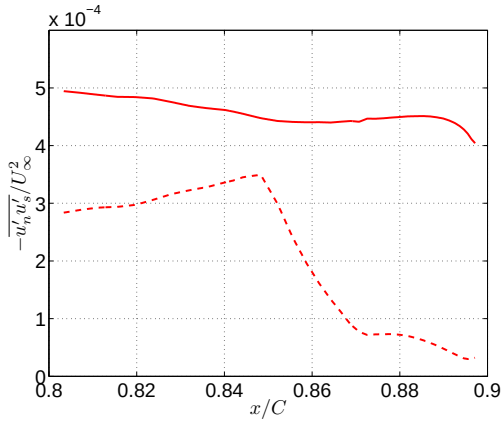

(a)

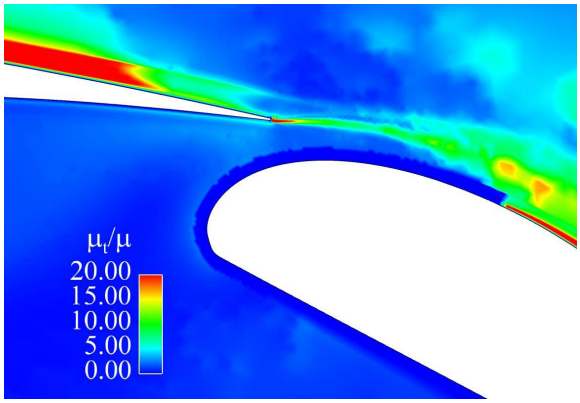

(b)

Figure 12. Modeled stress depletion on the trailing edge of the main wing for Case2. (a) Development of modeled and resolved shear stress along a grid line near the trailing edge (distance to the wall: $y/C \approx 0.0045$). ——: resolved, - - - - - -: modeled. (b) Contours of ν_t/ν showing the sudden reduction of eddy viscosity towards the trailing edge.

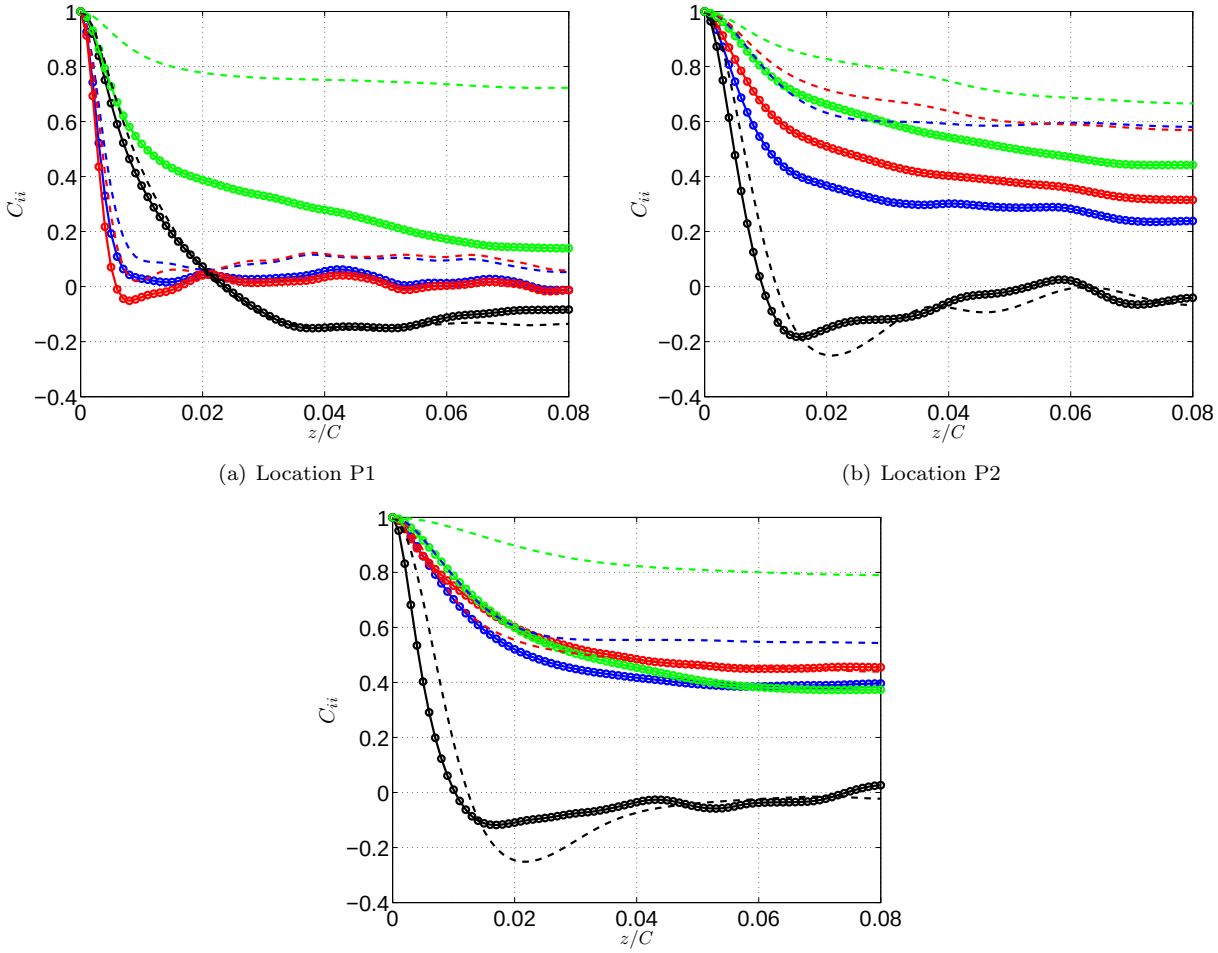

(a) Location P1

(b) Location P2

(c) Location P3

Figure 13. Spanwise two-point correlations in the slat cove region; dashed lines: Case1; solid lines: Case2; ——: $C_{uu,norm}$, ——: $C_{vv,norm}$, ——: $C_{ww,norm}$, ——: $C_{pp,norm}$. Markers on the lines indicate the spanwise resolution.

III.B. Aeroacoustic analysis

As only a small spanwise section of the high-lift wing is investigated here, the radiated noise levels are rather low. This makes it unnecessary to give absolute noise levels; hence, only the spacing is indicated on the y-axis (or r-axis in case of a polar plot). The noise radiation is computed at 72 observers located in a circle of radius 300 C around the airfoil. In the following, both the Sound Pressure Level (SPL) and the OverAll Sound Pressure Level (OASPL) for the different acoustic analogies will be presented. The Sound Pressure Level and the OASPL are defined as

$$SPL = 20 \log_{10} \left(\frac{p'}{p_{ref}} \right) \tag{10a}$$

$$OASPL = 20 \log_{10} \left(\frac{p_{rms}}{p_{ref}} \right) \tag{10b}$$

with p_{ref} being the reference pressure. In the present case, $p_{ref} = 2 \times 10^{-5}$ $[Pa]$ is chosen, which is usually considered the threshold of human hearing. An entire circle around the airfoil is computed so that it becomes possible to determine the direction in which the sound is mainly radiated. Figure 14 shows the polar coordinate system used and indicates that the upstream and downstream directions of the airfoil are aligned with the coordinates $\theta = 0°$ and $\theta = 180°$, respectively. The upward and downward directions then become $\theta = 90°$ and $\theta = 270°$, respectively.

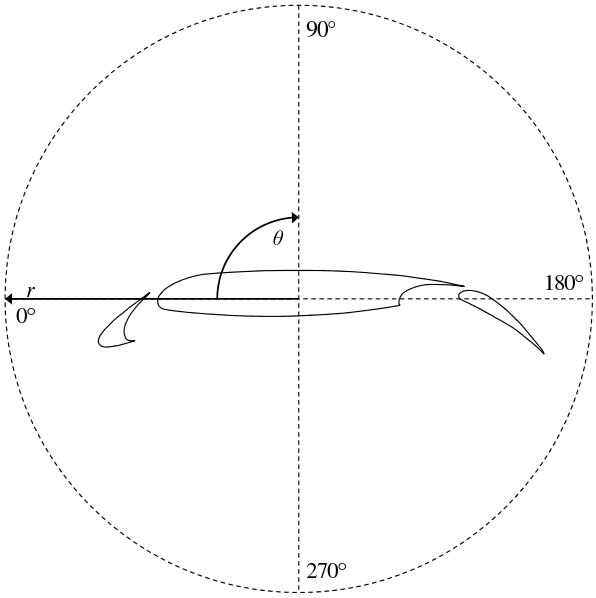

Figure 14. Polar coordinate-system

From a practical point of view, only the sound radiated in the downward direction, i.e. $\theta = 270°$, would be of interest. However, for completeness and for comparison, all 360 degrees are included in the directivity plots. Four observer locations at $\theta = 0°$, $\theta = 90°$, $\theta = 180°$ and $\theta = 270°$ were chosen for presenting the SPL plots. The SPL is plotted against the Strouhal number, $St = fC_s/U_\infty$, based on the slat chord, C_s. Please note that, in principle, the result at $\theta = 180°$ should be incorrect, as the downstream part of the integral surface is kept open.

III.B.1. Analysis using the Kirchhoff surface integral method

The SPL obtained with the Kirchhoff method are depicted in Fig. 15(a)– 15(d); included in the plots are both the SPL due to the components of the fluctuating pressure, $p'_{i,K}$, and the SPL due to their sum, $p'_{total,K}$. In general a broad-banded spectrum is obtained, which peaks at low Strouhal numbers for $St < 5$. Moreover, at Strouhal numbers in the range of $St \approx 1$–6, several narrow-banded tonal peaks are present. Several other research groups have also found the peak SPL levels around Strouhal numbers of $St \approx 1$–3 and

confirm the presence of tonal peaks in the low-frequency range.[3,11,8] The downward direction exhibits the strongest tonal peak at $St \approx 2.8$, with adjacent peaks at $St \approx 1.9$, $St \approx 3.6$ and $St \approx 4.5$. In comparison to previous near-field noise studies on this geometry,[36] there are more tonal peaks present that are shifted towards slightly higher frequencies. At $St \approx 40$, the spectra exhibits a broad-banded peak. It is most obvious in the upstream and downstream directions but can also be observed in the other two directions. A similar peak has been reported previously by several authors, for example, Choudhari et al.[45] and Khorrami.[46] It is the major source of high-frequency slat noise and is believed to stem from vortex shedding behind the blunt trailing edge of the slat. Further evidence for this hypothesis can be provided when plotting the spectra in Fig. 15 versus a Strouhal number based on the trailing edge thickness of the slat, St_{TE} (not shown). In that case, the peak appears at $St_{TE} \approx 0.12$, which is of the same order of magnitude as the frequency commonly associated with vortex shedding behind circular cylinders, $St_{cyl} \approx 0.2$.[47] Hence, the peak is indeed related to vortex shedding behind the blunt trailing edge of the slat. In previous research on another three-element airfoil at higher Reynolds numbers,[7,14] this peak appears at higher frequencies and is often shown to be the highest peak in the spectrum, which is not the case here. These differences can be attributed to the disparity of the investigated airfoils along with their test conditions.

At all four positions, $p'_{1,K}$ gives by far the smallest amplitude and does not significantly contribute to the total noise, $p'_{total,K}$. It is hence excluded from the plots in Fig. 15. Both, $p'_{2,K}$ and $p'_{3,K}$ follow the total noise quite well.

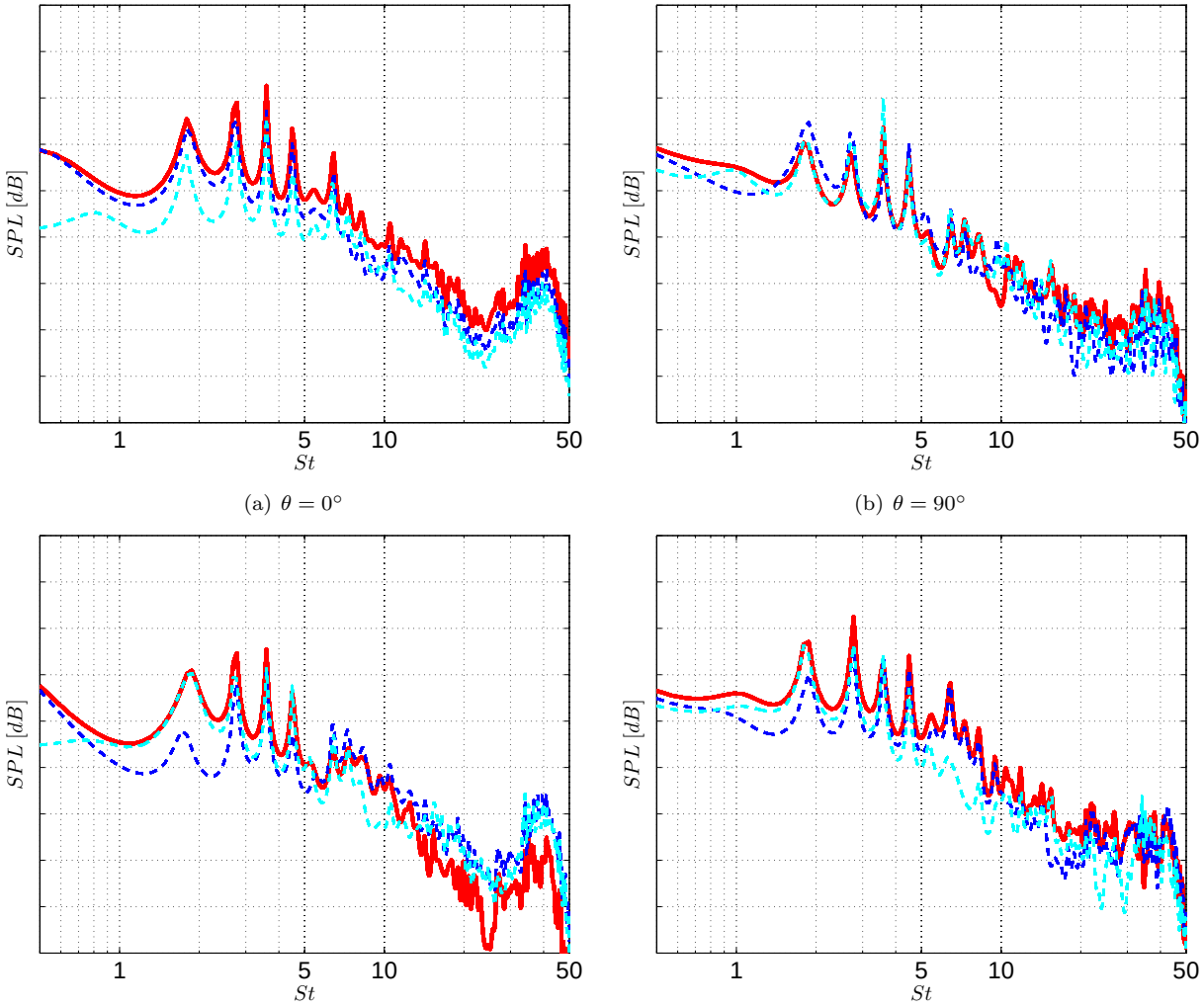

(a) $\theta = 0°$ (b) $\theta = 90°$

(c) $\theta = 180°$ (d) $\theta = 270°$

Figure 15. SPL for the Kirchhoff integral method. ——: $p'_{total,K}$, - - - -: $p'_{2,K}$, - - - -: $p'_{3,K}$. $\Delta SPL = 10$ [dB].

It is displayed in Fig. 16(a) that the Kirchhoff method predicts the total sound to behave like a monopole.

The largest contributor to the total noise is term 2 (Eq. (3b)), which is not surprising as $p'_{1,K}$ and $p'_{3,K}$ decrease with the cube and square of the observer distance, respectively (see Eqs. (3a) and (3c)). Yao and co-workers[10] show that the noise due to term 3 behaves like a dipole with radiation roughly in the $\theta = 100°$ and $\theta = 280°$ directions. Only weak dipole trends with radiation maxima roughly in the $\theta = 80°$ and $\theta = 240°$ directions can be observed here, but it is likely that the present high-lift configuration with an additional slat behaves differently than the one investigated by Yao and co-workers. The shaky behavior of $p'_{3,K}$ in the downstream direction might be caused by the fact that the integral surface is kept open in that direction. It is however evident that the source term directly connected with the pressure fluctuations, $p'_{1,K}$, exhibits a dipole emission, but at the same time does not play an important role in the overall sound.

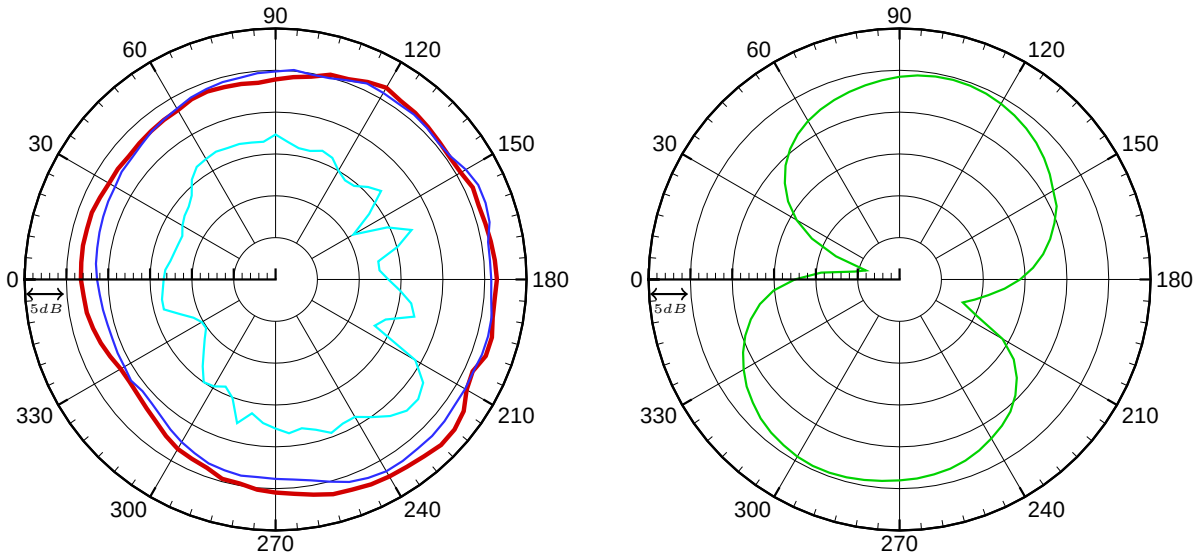

Figure 16. OASPL for the Kirchhoff integral method. (a) The total sound pressure along with $p'_{2,K}$ and $p'_{3,K}$ is shown. (b) Note that the scaling of the radial axis has changed. $p'_{1,K}$ is depicted separately, as its amplitude is significantly smaller than the other terms. ——: $p'_{total,K}$, ——: $p'_{1,K}$, ——: $p'_{2,K}$, ——: $p'_{3,K}$.

III.B.2. Analysis using the FWH method

Figure 17 presents the SPL obtained with the FWH method on the permeable and stationary surface. The contributions of the three surface integrals defined by Eq. (6) and the total sound pressure are included in the plots. Similar to the results obtained with the Kirchhoff integral method, a broad-banded spectrum with narrow-banded tonal peaks is shown, and the previously mentioned high-frequency peak at $St \approx 40$ can also be identified. The sound pressure due to the second term, $p'_{2,F}$, consistently yields the lowest levels with the weakest signal in the upward and downward directions. Recall that $p'_{2,F}$ is related to the momentum perturbations at the surface. One can then conclude that the momentum perturbations at the surface location are in general low. It can be seen that $p'_{1,F}$ closely follows the total sound pressure, $p'_{total,F}$, but that it does not represent the high-frequency peak. Contrary, this means that the high-frequency peak is associated solely with $p'_{3,F}$ and hence can be connected to the perturbations of mass through the surface, as made clear by Eq. (6c).

The directivity plots obtained by the FWH analogy are displayed in Fig. 18. They do not show a clear trend towards one of the acoustical source types but can rather be described as a superposition of different sources. Three flat radiation maxima can be found for $\theta \approx 30°$, $\theta \approx 180°$ and $\theta \approx 240°$, which correlates well with Lockard's[8] observations for a similar high-lift airfoil using the FWH analogy on a stationary, permeable surface at a distance of 10 C. In Fig. 17, $p'_{2,F}$ was found to be the smallest with the lowest sound pressure levels in the upward and downward directions. Figure 18(b) makes clear that $p'_{2,F}$ radiates like a dipole in the up- and downstream directions. Subsequently, the noise contribution of the momentum perturbations is not of practical importance in terms of noise reduction. When plotted in a different scaling (not shown here), $p'_{1,F}$ exhibits an emission of a dipole nature with maxima in the directions of $\theta \approx 80°$ and $\theta \approx 250°$.

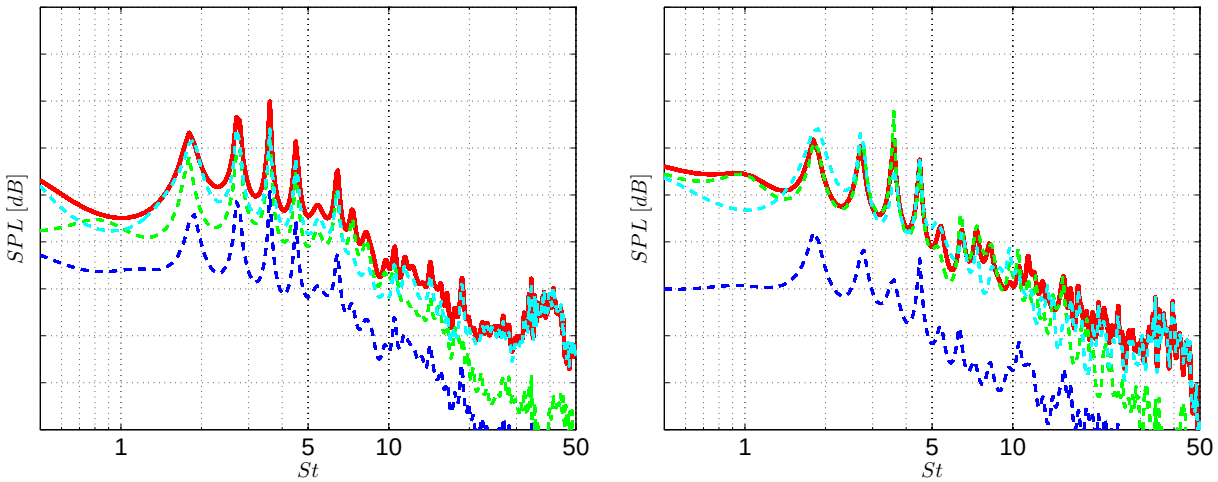

(a) $\theta = 0°$ (b) $\theta = 90°$

(c) $\theta = 180°$ (d) $\theta = 270°$

Figure 17. SPL obtained with the FWH method. ——: $p'_{total,F}$, - - - -: $p'_{1,F}$, - - - -: $p'_{2,F}$, - - - -: $p'_{3,F}$. $\Delta SPL = 10$ $[dB]$.

Thus, $p'_{1,F}$ and $p'_{2,F}$ radiate noise roughly orthogonal to each other. A similar behavior was observed by Yao et al.[10] for high-lift wings without a leading edge slat. In the range of $\theta \approx 210°$–$330°$, $p'_{1,F}$ is the dominant source of noise by roughly 2–5 $[dB]$, whereas in the up- and downstream directions $p'_{3,F}$ exceeds $p'_{1,F}$ by about 5 $[dB]$ and hence governs the total noise.

III.B.3. Analysis using Curle's method

The Curle method, as described earlier, only accounts for the pressure fluctuations at stationary, solid surfaces due to the flow. Hence, for the following analysis, the solid walls of the three elements of the airfoil, namely slat, wing and flap, are used. The total sound pressure, $p'_{total,C}$, corresponds in this case to the sum of the pressures of the three elements. This allows treating the noise radiation of each element in isolation.

The spectra displayed in Fig. 19 also exhibit a broad-banded shape for all of the elements and the total noise with peak levels in the range of $St \approx 1$–4. Besides the fact that the narrow-banded tonal peaks are present, the absence of the high-frequency peak is most obvious. As stated earlier, the high-frequency peak is associated with the perturbations of mass through the permeable surface, which is not accounted for in Curle's method. The slat claims the highest SPL amplitudes at all four observer locations presented. It has been widely acknowledged that the slat is indeed the major contributor to noise due to the high-lift system.[2,3,12,11,13] In the downward direction, the SPL plots indicate that the wing and flap do not

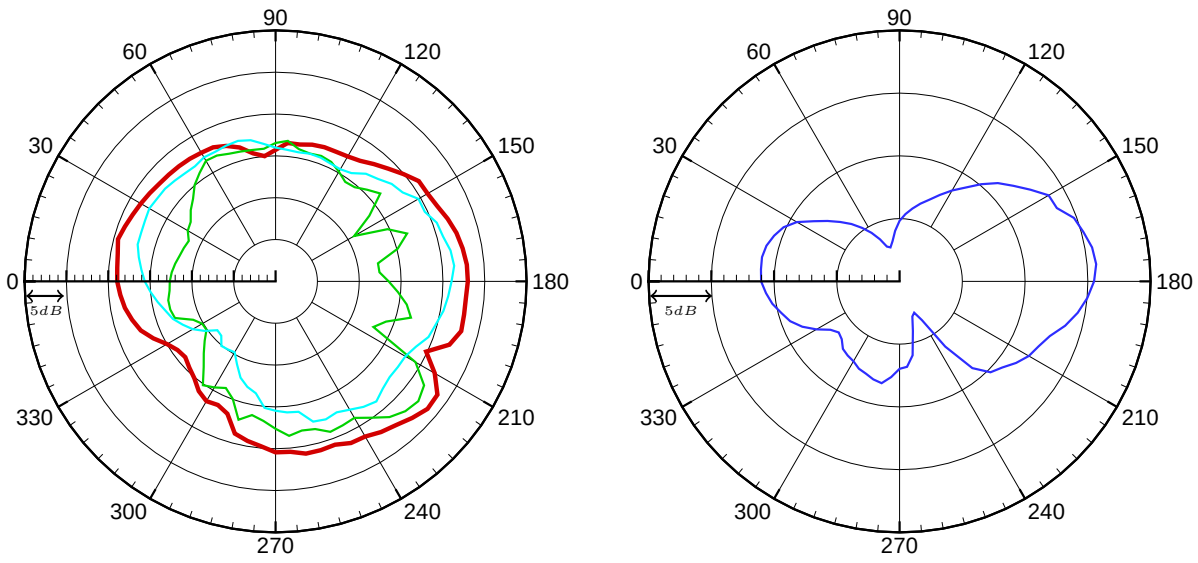

(a) (b)

Figure 18. OASPL for the FWH method. In (b), $p'_{2,F}$ is depicted separately, as it is smaller than the other terms. Note that the maximum of (b) corresponds to the 2nd lowest level in (a). ——: $p'_{total,F}$, ——: $p'_{1,F}$, ——: $p'_{2,F}$, ——: $p'_{3,F}$.

contribute to the total noise as much as the slat.

Figure 20 depicts the directivity plots for the three elements together with the OASPL of the total noise. The total noise has its radiation maxima in directions $\theta \approx 15°$ and $\theta \approx 230°$. It is evident that the slat radiates as a dipole and is the main contributor to the total noise. Exactly as with the total noise, the slat predominantly radiates into the upper forward arc ($\theta \approx 15°$) and in the lower rearward direction ($\theta \approx 230°$). The wing shows no distinct behavior but rather a superposition of different sources. However, the strongest emission is found in the direction of $\theta \approx 150°$. Except in that and in the opposite direction, the wing emits much lower levels than the slat and hence does not contribute considerably to the total sound pressure. Even though it is of low intensity, the flap exhibits an almost perfect dipole emission in the upper rearward direction ($\theta \approx 135°$) and the lower forward region ($\theta \approx 315°$). Recall that the slat and flap are deflected by 28.8° and 38.3° with respect to the θ-axis. It then becomes obvious that both slat and flap emit orthogonally to their own orientation. The wing could possibly be another superposition of two dipoles directed almost orthogonally to each other.

III.B.4. Comparison of the acoustic analogies

As the results obtained with the different acoustic analogies were generally similar, but deviations from each other were not negligible, a detailed comparison of the methods is carried out here.

Firstly, the Sound Pressure Levels obtained by the three acoustic analogies are compared in Fig. 21. The SPL of the three methods show similar spectra with the tonal peaks predicted at very similar frequencies. Table 2 gives the frequencies of the five tonal peaks, as indicated in Fig. 21(d). Curle's method predicts the tonal peaks at slightly lower Strouhal numbers than Kirchhoff's method. To the contrary, the FWH method gives slightly higher Strouhal numbers for the same peaks. In the frequency range shown, the three methods yield fairly similar amplitudes, which indicates that the major differences are located in the low-frequency region, $St < 1.5$.

The OASPL of the respective analogies are cross-plotted in Fig. 22. Note that the scaling has been changed in comparison to the previous OASPL plots in order to emphasize the differences. The Kirchhoff method consistently predicts the highest sound pressure levels, and Curle's method consistenly predicts the lowest levels, with the Ffowcs-Williams and Hawkings method in between the two. Deviations between the Curle and the Kirchhoff method are considerable and range from 5–10 $[dB]$. Even compared to the FWH method, Kirchhoff yields at least 4 $[dB]$ higher levels of sound pressure. The Kirchhoff method yields

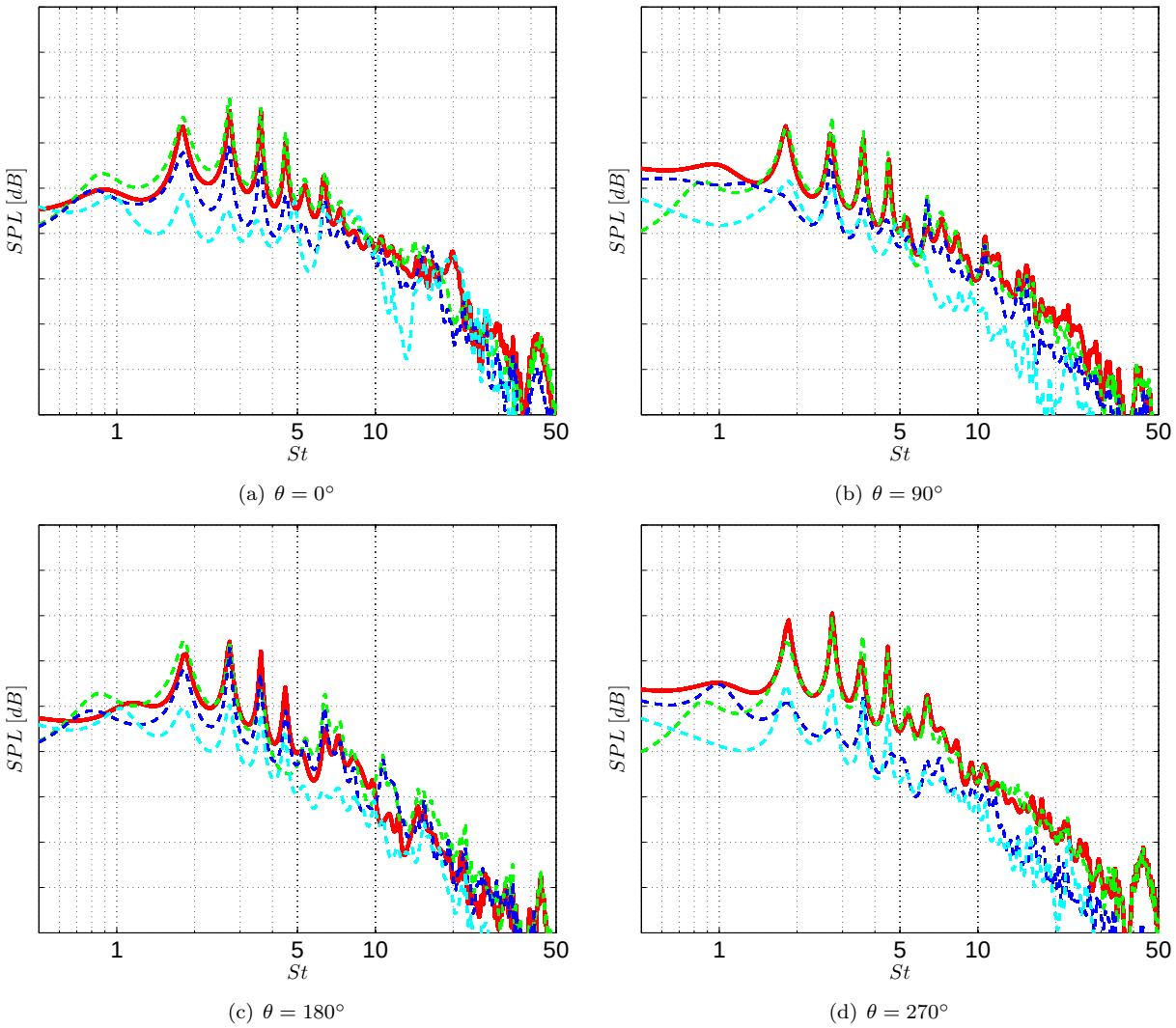

(a) $\theta = 0°$ (b) $\theta = 90°$

(c) $\theta = 180°$ (d) $\theta = 270°$

Figure 19. SPL obtained with the Curle method. ——: $p'_{total,C}$, - - - -: $p'_{slat,C}$, – – –: $p'_{wing,C}$, – - – -: $p'_{flap,C}$. $\Delta SPL = 10$ $[dB]$.

such high values due to $p'_{2,K}$, which is particularly high at low frequencies. Excluding this term from the calculation of the total noise results in noise levels comparable to the ones of the FWH and Curle methods (not presented here). The Curle analogy only takes into account the contribution of the pressure fluctuations at the solid walls of the airfoil. In the FWH method, the noise from the turbulence in the flow field is also involved, which helps to explain the differences observed between the two methods. Despite the deviations in amplitude, the Curle and FWH methods yield similar radiation patterns, which clearly highlights the likeness of the two approaches. It was explained earlier that the FWH method for a stationary surface would be identical to the Curle method if the airfoil's elements were chosen instead of the permeable surface. To further illustrate the similarity of the Curle and FWH methods, $p'_{1,F}$ in Fig. 17 is not able to represent the high-frequency peak, since it is identical to $p'_{total,C}$ in the Curle method.

Figures 16 and 18 reveal that $p'_{3,K}$ and $p'_{1,F}$ show almost identical results. By inspection of Eq. (6a), one can see that $p'_{1,F}$ is actually identical to the sum of $p'_{1,K}$ and $p'_{3,K}$ (Eq. (3)). It was shown earlier that $p'_{1,K}$ is negligible in the far-field, as it decreases with the cube of the observer distance. Hence, it is an expected outcome that $p'_{3,K}$ and $p'_{1,F}$ yield similar results.

Frequency spectra of the fluctuating pressure for the downward observer location are presented in Fig. 23. Note that, on the x-axis, the Strouhal number is plotted in logarithmic scale. On the y-axis, the Strouhal number multiplied with the power spectral density is plotted in linear scale. The energy content of a range of frequencies is hence characterized by the area under the curve. The tonal peaks at $St \approx 1.9$, $St \approx 2.8$,

Table 2. Strouhal numbers of tonal peaks

	Peak I	Peak II	Peak III	Peak IV	Peak V
	St	St	St	St	St
Kirchhoff	1.84	2.77	3.59	4.49	6.40
Curle	1.86	2.73	3.56	4.49	6.37
FWH	1.84	2.78	3.60	4.50	6.42

$St \approx 3.6$ and $St \approx 4.5$ can be recognized. By far the most energetic peak is located at $St \approx 2.8$. One can observe that, at almost all frequencies, the moste energetic peaks are obtained with the Kirchhoff and FWH methods, which is consistent with the indications of the SPL and OASPL plots above.

A broad-banded peak at large Strouhal numbers was presented in Figs. 15 and 17, particularly for the upstream and downstream directions. Despite the fact that those two directions are of limited practical interest, the Strouhal number spectrum for the $\theta = 0°$ direction is given in Fig. 24. Even though the spectrum is dominated by the large peaks at low Strouhal numbers, some peaks with large energy can be identified at Strouhal numbers of $St \approx 35$–45. As highlighted in the zoom-up of the high-frequency peaks presented in Fig. 24(b), the Kirchhoff method yields higher peaks and a larger contribution to the total noise than the FWH method. Moreover, one can observe that no peaks can be identified for the Curle analogy, as expected from Fig. 19.

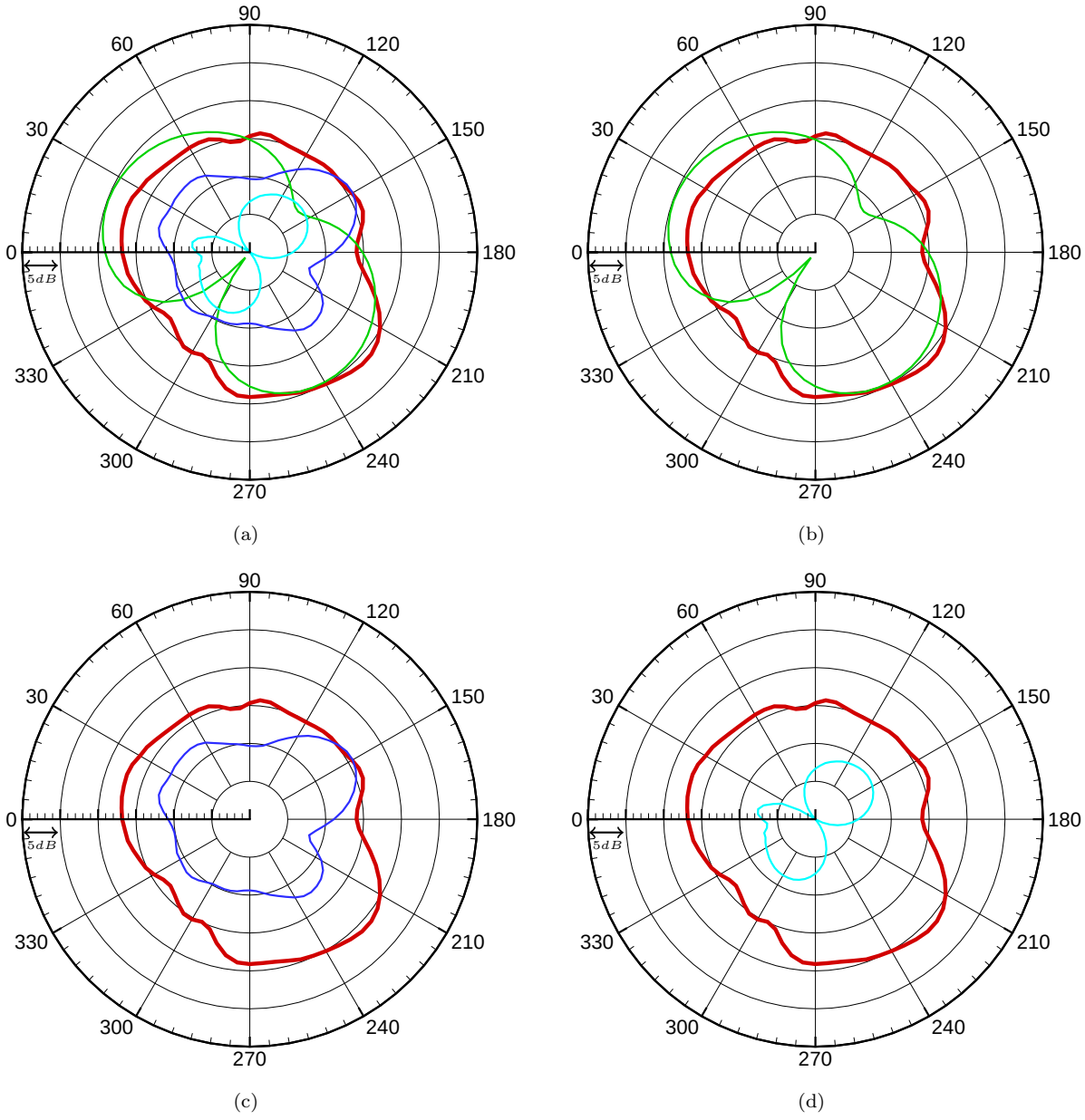

(a) (b)

(c) (d)

Figure 20. OASPL for the Curle method. ——: $p'_{total,C}$, ——: $p'_{slat,C}$, ——: $p'_{wing,C}$, ——: $p'_{flap,C}$.

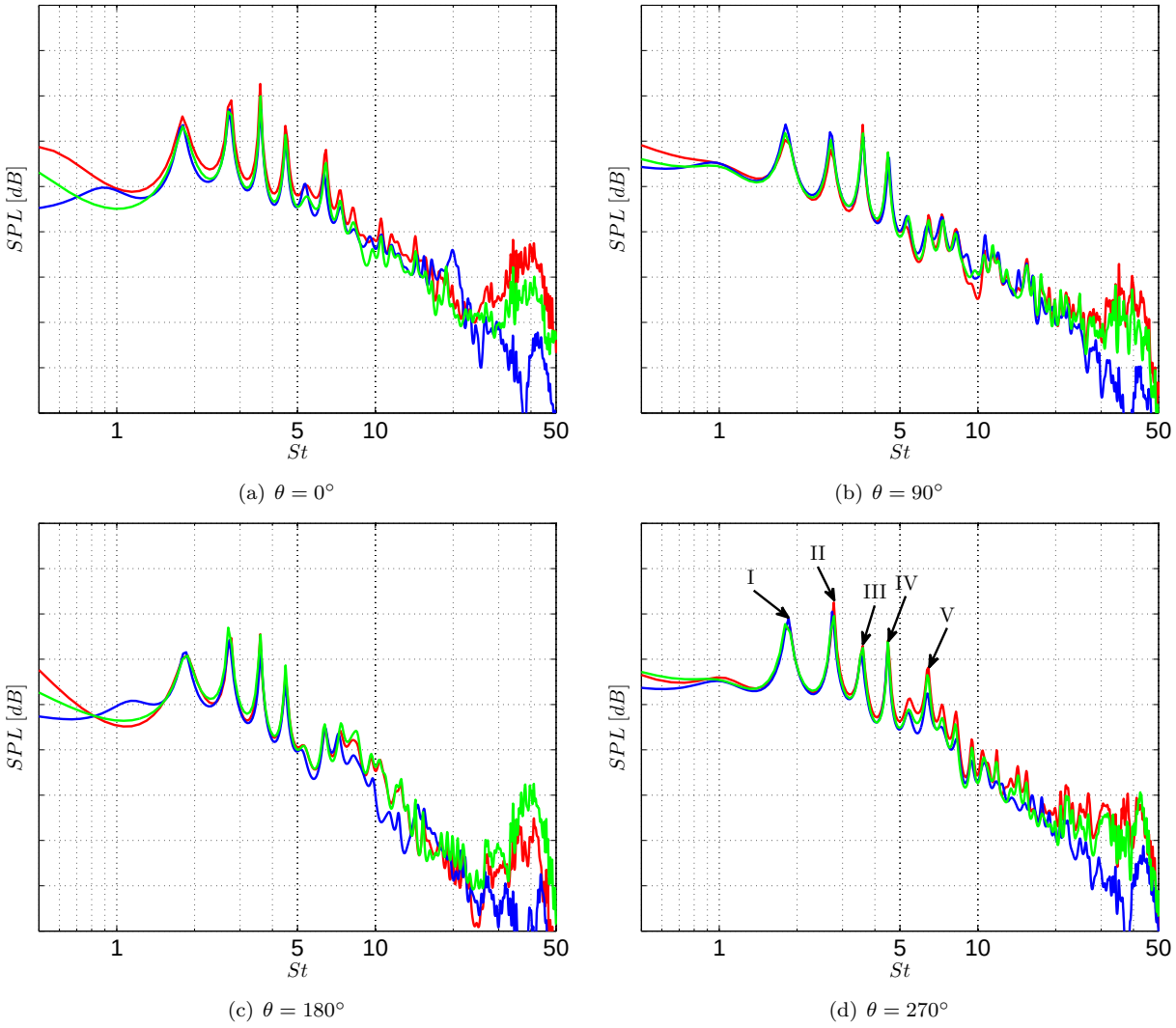

(a) $\theta = 0°$

(b) $\theta = 90°$

(c) $\theta = 180°$

(d) $\theta = 270°$

Figure 21. Comparison of the SPL obtained with different acoustic analogies. ——: Kirchhoff, ——: Curle, ——: FWH. $\Delta SPL = 10\ [dB]$.

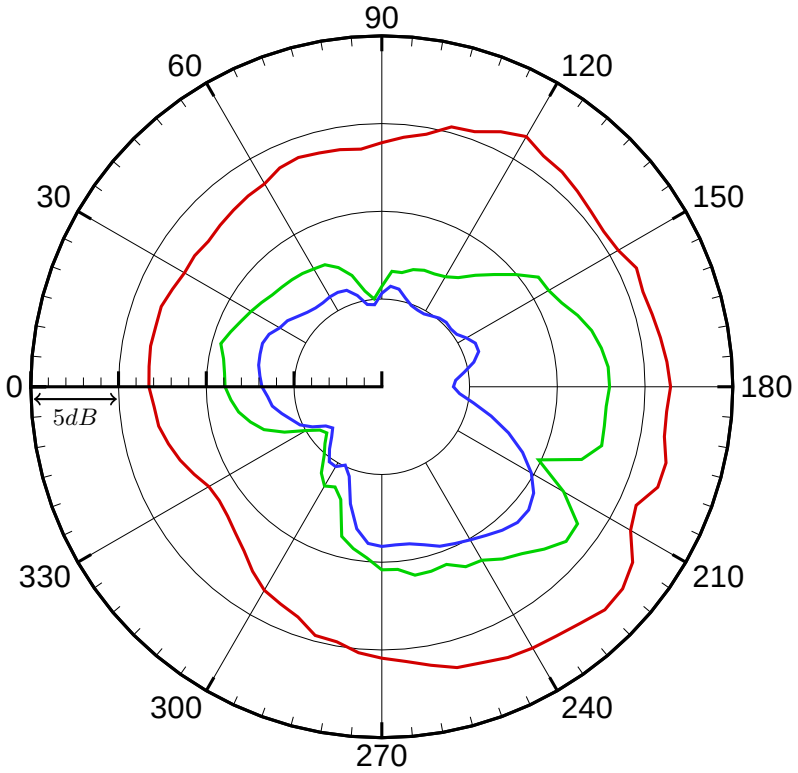

(a)

Figure 22. OASPL for the three acoustic analogies. ——: Kirchhoff, ——: Curle, ——: FWH

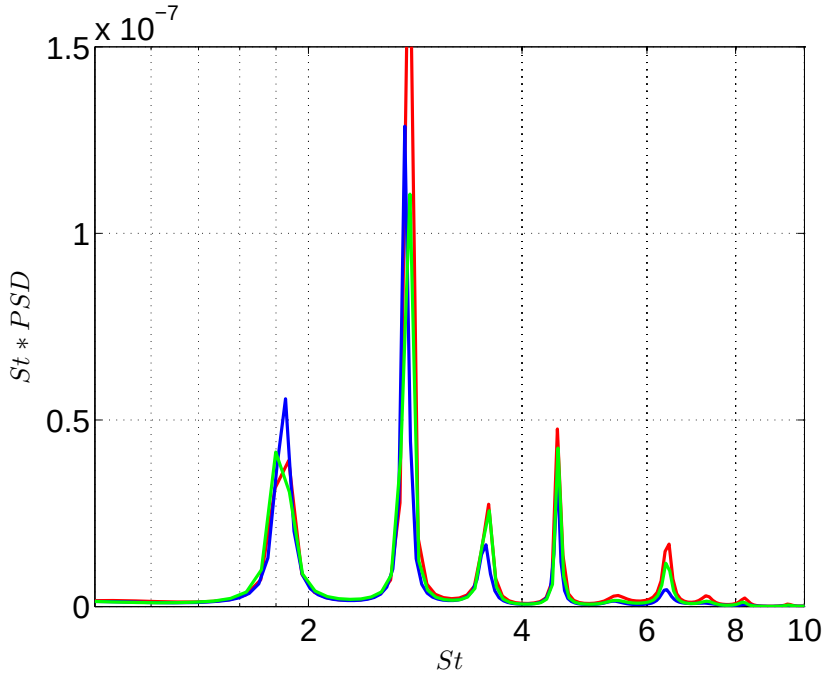

(a)

Figure 23. Energy spectrum of the sound pressure at $\theta = 270°$. ——: Kirchhoff, ——: Curle, ——: FWH

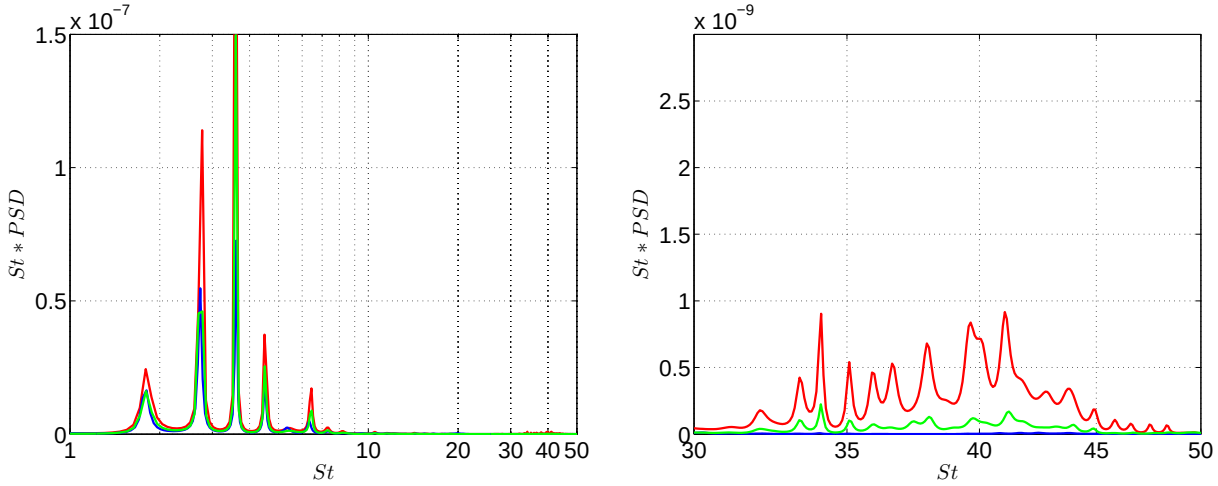

(a) entire spectrum

(b) zoom-in

Figure 24. Energy spectrum of the sound pressure at $\theta = 0^\circ$. ——: Kirchhoff, ——: Curle, ——: FWH

IV. Conclusion

The complex flow around a three-element high-lift airfoil configuration was investigated with the help of a hybrid RANS/LES modeling approach based on a simple algebraic RANS formulation. The pressure distribution around the three elements of the airfoil are in good agreement with experimental data. Due to the use of a finer grid in the $x - y$ plane, Kelvin-Helmholtz instabilities are observed almost immediately after the slat cusp, proving the superiority of the refined grid compared to the grid used in a previous study. However, secondary instabilities leading to fully three-dimensional turbulence in the shear layer are still considerably delayed. Because of this, the levels of resolved turbulent kinetic energy in the shear layer are still low in comparison with results shown by other research groups. Two-point correlations in the spanwise direction indicate that an even larger spanwise domain extent than 16% C would be desirable. The hybrid model used has proved to be generally capable of predicting the flow around a high-lift airfoil. The current work is further evidence of the fact that, with the help of hybrid RANS/LES modeling, turbulence resolving methods are becoming more and more feasible for industrial applications.

An acoustic analysis of the far-field noise involving three acoustic analogies, namely, the Kirchhoff, the Ffowcs-Williams and Hawkings and the Curle method, has been performed. The input data for the Kirchhoff and Ffowcs-Williams and Hawkings methods has been sampled at a stationary, but permeable integral surface. All three methods agree well in terms of the frequencies at which tonal noise has been predicted. Using the Kirchhoff and FWH analogies, it was possible to capture the broad-banded high-frequency peak, which is typically associated with vortex shedding from the blunt slat trailing edge. The Kirchhoff method was found to predict considerably higher noise levels than the other two methods. Once again, the slat could be established as the main contributor to airframe noise of high-lift airfoils. It was furthermore shown that both the slat and the flap radiate noise in a dipole fashion in the directions orthogonal to their own orientation.

Moreover, the aeroacoustic strategy was based on decoupling the flow computations from the acoustic calculations. In that way, it was shown that turbulence resolving methods are now ready to be employed in the acoustic analysis of even complex geometries.

V. Acknowledgments

The financial support of SNIC (the Swedish National Infrastructure for Computing) for computer time at C3SE (Chalmers Center for Computational Science and Engineering) is gratefully acknowledged. The authors also want to express their gratitude to PDC (Center for High Performance Computing) at KTH Stockholm for allocated computer time. This project was financed by the EU project ATAAC (Advanced Turbulence Simulation for Aerodynamic Application Challenges), Grant Agreement No. 233710. The ATAAC project is described at `http://cfd.mace.manchester.ac.uk/ATAAC/WebHome`

References

[1]ORGANIZATION, I. C. A., *Annex 16 to the Convention on International Civil Aviation, Volume 1 Aircraft Noise*, ICAO, 4th ed., 2005.

[2]Dobrzynski, W., Nagakura, K., Gehlhar, B., and Buschbaum, A., "Airframe Noise Studies on Wings with Deployed High-Lift Devices," *4th AIAA/CEAS Aeroacoustics Conference*, Toulouse, France, 2-4 June 1998, AIAA paper 98-2337.

[3]Dobrzynski, W. and Pott-Pollenske, M., "Slat Noise Source Studies for FarField Noise Prediction," *7th AIAA/CEAS Aeroacoustics Conference*, Maastricht, The Netherlands, 28-30 May 2001, AIAA paper 2001-2158.

[4]Dobrzynski, W., Gehlhar, B., and Buchholz, H., "Model and full scale high-lift wing wind tunnel experiments dedicated to airframe noise reduction," *Aerospace Science and Technology*, Vol. 5, 2001, pp. 27–33.

[5]Guo, Y. and Joshi, M., "Noise Characteristics of Aircraft High-Lift Systems," *AIAA Journal*, Vol. 41, 2003, pp. 1247–1256.

[6]Chow, L., Mau, K., and Remy, H., "Landing Gears and High Lift Devices Airframe Noise Research," *8th AIAA/CEAS Aeroacoustics Conference and Exhibit*, Breckenridge, USA, 17-19 June 2002, AIAA paper 2002-2408.

[7]Singer, B., Lockard, D., and Brentner, K., "Computational Aeroacoustic Analysis of Slat Trailing-Edge Flow," *AIAA Journal*, Vol. 38, 2000, pp. 1558–1564.

[8]Lockard, D. and Choudhari, M., "Noise Radiation from a Leading-Edge Slat," *15th AIAA Aeroacoustics Conference*, Miami, USA, 11-13 May 2009, AIAA paper 2009-3101.

[9]Yao, H.-D., Eriksson, L.-E., Davidson, L., Grundestam, O., Peng, S.-H., and Eliasson, P., "Aeroacoustic Assessment of Conceptual Low-Noise High-Lift Wing Configurations," *50th AIAA Aerospace Sciences Meeting incl. the New Horizons Forum and Aerospace Exposition*, Nashville, USA, 09-12 January 2012, AIAA paper 2012-0383.

[10]Yao, H.-D., Davidson, L., Eriksson, L.-E., Grundestam, O., Peng, S.-H., and Eliasson, P., "Surface Integral Analogy Approaches to Computing Noise Generated by a 3D High-Lift Wing Configuration," *50th AIAA Aerospace Sciences Meeting incl. the New Horizons Forum and Aerospace Exposition*, Nashville, USA, 09-12 January 2012, AIAA paper 2012-0386.

[11]Choudhari, M. and Khorrami, M., "Effect of Three-Dimensional Shear-Layer Structures on Slat Cove Unsteadiness," *AIAA Journal*, Vol. 45, 2007, pp. 2174–2186.

[12]Wild, J., Pott-Pollenske, M., and Nagel, B., "An integrated design approach for low noise exposing high-lift devices," *3rd AIAA Flow Control Conference*, San Francisco, USA, 2006, AIAA paper 2006-2843.

[13]Wild, J., Wichmann, G., Haucke, F., Peltzer, I., and Scholz, P., "Large scale separation flow control experiments within the German Flow Control Network," *47th AIAA Aerospace Sciences Meeting*, Orlando, USA, 2009, AIAA paper 2009-0530.

[14]Khorrami, M., Berkman, M., and Choudhari, M., "Unsteady Flow Computations of a Slat with a Blunt Trailing Edge," *AIAA Journal*, Vol. 38, 2000, pp. 2050–2058.

[15]Jenkins, L., Khorrami, M., and Choudhari, M., "Characterization of Unsteady Flow Structures Near Leading-Edge Slat: Part I. PIV Measurements," *10th AIAA Aeroacoustics Conference*, Manchester, UK, 10-12 May 2004, AIAA paper 2004-2801.

[16]Khorrami, M., Choudhari, M., and Jenkins, L., "Characterization of Unsteady Flow Structures Near Leading-Edge Slat: Part II. 2D Computations," *10th AIAA Aeroacoustics Conference*, Manchester, UK, 10-12 May 2004.

[17]Olson, S., Thomas, F., and Nelson, R., "A Preliminary Investigation into Slat Noise Production Mechanisms in a High-Lift Configuration," *18th AIAA Applied Aerodynamics Conference*, Denver, USA, 14-17 August 2000, AIAA paper 2000-4508.

[18]Storms, B., Hayes, J., Ross, J., and Moriarty, P., "Aeroacoustic measurements of slat noise on a three-dimensional high-lift system," *5th AIAA/CEAS Aeroacoustics Conference*, Greater Seattle, USA, 10-12 May 1999, AIAA paper 99-1957.

[19]Spalart, P., Jou, W.-H., Strelets, M., and Allmaras, S., "Comments on the Feasibility of LES for Wings and on a Hybrid RANS/LES Approach," *Proceedings of the First AFOSR International Conference on DNS/LES*, Greyden Press, Ruston, USA, 1997, pp. 137–147.

[20]Deck, S., "Zonal-Detached-Eddy Simulation of the Flow Around a High-Lift Configuration," *AIAA Journal*, Vol. 43, 2005, pp. 2372–2384.

[21]Deck, S., "Recent improvements in the Zonal Detached Eddy Simulation (ZDES) formulation," *Theor. Comput. Fluid Dyn.*, 2011, pp. 1–28, 10.1007/s00162-011-0240-z.

[22]Deck, S., "Numerical Simulation of Transonic Buffet over a Supercritical Airfoil," *AIAA Journal*, Vol. 43, 2005, pp. 1556–1566.

[23]Menter, F., "Two-Equation Eddy-Viscosity Turbulence Models for Engineering Applications," *AIAA Journal*, Vol. 32, 1994, pp. 1598–1605.

[24]Menter, F., Kuntz, M., and Langtry, R., "Ten Years of Industrial Experience with the SST Turbulence Model," *Turbulence, Heat and Mass Transfer 4*, edited by K. Hanjalic, Y. Nagano, and M. Tummers, Begell House, Antalya, Turkey, 2003.

[25]Margolin, L. and Rider, W., "The design and construction of implicit LES models," *International Journal for Numerical Methods in Fluids*, Vol. 47, No. 10-11, 2004, pp. 1173–1179, DOI: 10.1002/fld.862.

[26]Margolin, L., Rider, W., and Grinstein, F., "Modeling turbulent flow with implicit LES," *Journal of Turbulence*, Vol. 7, No. 15, 2006.

[27]Aspden, A., Nikiforakis, N., Dalziel, S., and Bell, J., "Analysis of Implicit LES Methods," *Communications in Applied Mathematics and Computational Science*, Vol. 3, No. 1, 2008, pp. 103–126.

[28]Peng, S.-H., "Hybrid RANS-LES Modeling based on Zero- and One-Equation Models for Turbulent Flow Simulation," *Proceedings of 4th International Symposium on Turbulence and Shear Flow Phenomena*, Vol. 3, Williamsburg, USA, 27-29 June 2005, pp. 1159–1164.

[29]Peng, S.-H., "Algebraic Hybrid RANS-LES Modelling Applied to Incompressible and Compressible Turbulent Flows," *36th Fluid Dynamics Conference and Exhibit*, San Francisco, USA, 5-8 June 2006, AIAA paper 2006-3910.

[30]Farassat, F. and Myers, M., "Extension of Kirchhoff's Formula to Radiation from Moving Surfaces," *Journal of Sound and Vibration*, Vol. 123, 1988, pp. 451–460.

[31]Ffowcs-Williams, J. and Hawkings, D., "Sound Generation by Turbulence and Surfaces in Arbitrary Motion," *Philosophical Transactions of the Royal Society*, Vol. 264, 1969, pp. 321–342.

[32]Brentner, K. and Farassat, F., "Modeling aerodynamically generated sound of helicopter rotors," *Progress in Aerospace Sciences*, Vol. 39, 2003, pp. 83–120.

[33]Curle, N., "The influence of solid boundaries upon aerodynamic sound," *Proceedings of the Royal Society of London. Series A, Mathematical and Physical Sciences*, Vol. 231, 1955, pp. 505–514.

[34]Smagorinsky, J., "General Circulation Experiments with the Primitive Equations," *Monthly Weather Review*, Vol. 91, 1963, pp. 99–164.

[35]Nebenführ, B., Peng, S.-H., and Davidson, L., "Precursor RANS computations for the F15 three-element high-lift configuration," Tech. Rep. FOI Memo 2865, Chalmers/FOI, 2010.

[36]Nebenführ, B., Peng, S.-H., and Davidson, L., "Hybrid RANS-LES Simulation of Turbulent High-Lift Flow in Relation to Noise Generation," *Progress in Hybrid RANS-LES Modelling, NNFM*, edited by S. F. et al., Vol. 117, Springer, 2012, pp. 303–314.

[37]Kirchhoff, G., "Zur Theorie der Lichstrahlen," *Annalen der Physik*, Vol. 254, 1883, pp. 663–695.

[38]Lyrintzis, A., "Review: The Use of Kirchhoff's Method in Computational Aeroacoustics," *Journal of Fluids Engineering*, Vol. 116, 1994, pp. 665–676.

[39]Lighthill, M., "On Sound Generated Aerodynamically. I. General Theory," *Proceedings of the Royal Society of London. Series A, Mathematical and Physical Sciences*, Vol. 211, 1952, pp. 564–587.

[40]Lighthill, M., "On Sound Generated Aerodynamically. II. Turbulence As A Source Of Sound," *Proceedings of the Royal Society of London. Series A, Mathematical and Physical Sciences*, Vol. 222, 1954, pp. 1–32.

[41]Brentner, K. and Farassat, F., "An Analytical Comparison of the Acoustic Analogy and Kirchhoff Formulation for Moving Surfaces," *AIAA Journal*, Vol. 336, 1998, pp. 1379–1386.

[42]Spalart, P., "Detached-Eddy Simulation," *Annual Reviews of Fluid Mechanics*, Vol. 41, 2009, pp. 181–202.

[43]Menter, F. and Kuntz, M., "Adaption of eddy-viscosity turbulence models to unsteady separated flow behind vehicles," *Symposium on the aerodynamics of heavy vehicles: trucks, buses and trains.*, edited by R. McCallen, F. Browand, and J. Ross, Springer, Monterey, USA, 2-6 December 2002.

[44]Davidson, L., "Large Eddy Simulations: How to evaluate resolution," *International Journal of Heat and Fluid Flow*, Vol. 30, 2009, pp. 1016–1025.

[45]Choudhari, M., Lockard, D., Macaraeg, M., Singer, B., Streett, C., Neubert, G., Stoker, R., Underbrink, J., Berkman, M., Khorrami, M., and Sadowski, S., *Aeroacoustic Experiments in the Langley Low-Turbulence Pressure Tunnel*, 2002, NASA/TM-2002-211432.

[46]Khorrami, M., "Understanding Slat Noise Sources," *Computational Aeroacoustics: From Acoustic Sources Modeling to Far-Field Radiated Noise Prediction Colloquium EUROMECH 449*, Chamonix, France, 9-12 December 2003.

[47]Norberg, C., "An experimental investigation of the flow around a circular cylinder: influence of aspect ratio," *Journal of Fluid Mechanics*, Vol. 258, 1994, pp. 287–316, doi:10.1017/S0022112094003332.